The Effect of Temperature Distribution during Laser Heat Treatment of Gas-Nitrided 42CrMo4 Steel on the Microstructure and Mechanical Properties

Dominika Panfil-Pryka [1] , **Michal Kulka** [1,*], **Natalia Makuch** [1], **Jerzy Michalski** [2] **and Piotr Dziarski** [1]

[1]   Institute of Materials Science and Engineering, Poznan University of Technology, Pl. M.Sklodowskiej-Curie 5, 60-965 Poznan, Poland; dominika.panfil-pryka@put.poznan.pl (D.P.-P.); natalia.makuch@put.poznan.pl (N.M.); piotr.dziarski@put.poznan.pl (P.D.)

[2]   Department of Materials Engineering, Czestochowa University of Technology, Al. Armii Krajowej 19, 42-200 Częstochowa, Poland; jerzymichalski987@gmail.com

*   Correspondence: michal.kulka@put.poznan.pl; Tel.: +48-61-6653575

Abstract: A gas-nitrided layer was produced on the toughened 42CrMo4 low-alloy steel using the changeable nitriding potential in order to limit the thickness of a brittle ε zone. The microstructure consisted of the compound $\varepsilon + (\varepsilon + \gamma')$ zone and diffusion zone (nitric sorbite with γ' precipitates). Such a layer was subjected to laser heat treatment with or without remelting. The single laser tracks were formed using various laser beam powers (in the range of 0.234–0.624 kW) and scanning rates (in the range of 2.24–3.84 m·min^{-1}) and the same laser beam diameter (2 mm). The microstructure of laser-modified nitrided layer usually consisted of re-melted zone (MZ) with coarse-grained nitric martensite Fe$_{\alpha'}$ and possible ε precipitates, heat-affected zone (HAZ) with fine-grained nitric martensite Fe$_{\alpha'}$ and γ' precipitates and diffusion zone with nitric sorbite and γ' precipitates. Sometimes, the compound zone was partially re-melted and an amount of iron nitrides remained in the MZ. Only one laser track was characterized by the different microstructure, consisting of the compound $\varepsilon + (\varepsilon + \gamma')$ zone, HAZ with fine-grained nitric martensite Fe$_{\alpha'}$ and γ' precipitates and diffusion zone with nitric sorbite and γ' precipitates. This laser track was formed without visible effects of remelting. The effect of temperature distribution during laser heat treatment of gas-nitrided 42CrMo4 steel on the microstructure and mechanical properties was studied. The equations developed by Ashby and Esterling were used in order to determine the temperature distribution along the axis of each laser track. Taking into account the temperature profiles, it was possible to calculate the depths of MZ and HAZ. These predicted values were compared to those-measured based on the microstructure observations, obtaining good compatibility. The microstructure of the produced surface layers influenced the mechanical properties such as hardness and Young's modulus. The hardness of MZ was higher than that of ε zone and lower than that of $\varepsilon + \gamma'$ zone when compared to nitrided layer. Whereas Young's modulus of MZ was significantly higher than those characteristic of the compound zone in gas-nitrided layer (both ε and $\varepsilon + \gamma'$ zone) and similar to that of HAZ. The laser heat treatment (LHT) without remelting resulted in the similar hardness and slightly higher Young's modulus of ε zone in comparison with the nitrided layer. Simultaneously, such a treatment of the nitrided layer did not influence the hardness and the Young's modulus of $\varepsilon + \gamma'$ zone considerably. The hardness of HAZ was higher than that of MZ and that of the same area of diffusion zone in the nitrided layer because of the presence of fine-grained nitric martensite with γ' precipitates after laser quenching.

Keywords: gas nitriding; compound zone; laser heat treatment; temperature distribution; microstructure; hardness; Young's modulus

1. Introduction

Nitriding process is well-known as a technique of surface treatment that improves the mechanical properties of metallic materials [1]. The most common methods of nitriding are as follows: controlled gas nitriding [2–6], plasma nitriding [7–12], and low-pressure gas nitriding [13,14]. Controlled gas nitriding and low-pressure gas nitriding is commonly used for constructional and tool steels. Plasma nitriding, also called ionic nitriding or nitriding under glow discharge conditions, can be also used for these steels. However, plasma process is particularly suitable for materials that are susceptible to passivation. Therefore, such materials as high-alloy steels [11], nickel alloys [7], or titanium alloys [9] are usually subjected to plasma nitriding.

The typical gas nitriding of steels often caused an unfavorable increase in the thickness of the compound zone close to the surface. The presence of thick and porous ε ($Fe_{2-3}N$) iron nitrides was particularly inadvisable. Therefore, in recent years, controlled gas nitriding has been intensively developed [2–6]. The process parameters, characteristic of the nitriding atmosphere, were as follows: the nitriding potential (K_N), the ammonia dissociation rate (α), the percentage composition of gaseous components of the atmosphere, and the flow rate (F_{In}). Such a process enabled the control and regulation of the growth of the nitrided layer using the changeable value of the nitriding potential [2,3,6]. It also guaranteed the repeatability of the phase composition at specified nitriding parameters. The possible microstructure of compound zone could be as follows: ε + (ε + γ') iron nitrides with a predominant percentage of ε phase, ε + γ' iron nitrides with a lesser percentage of ε phase and only γ' (Fe_4N) iron nitrides at the surface [3]. The nitriding potential was used to control the kinetics of the nitriding process. Its suitable selection was very important to control not only the growth kinetics of the diffusion zone, but also the thickness and phase composition of the iron nitride zone (compound zone) [2,3,6,15]. Phase composition of the compound zone (with iron nitrides) strongly influenced the hardness of the layer close to the surface. The reduced hardness was observed if a porous ε iron nitrides appeared on the surface [3]. The significant acceleration in the growth kinetics of the gas-nitrided layer was observed due to the increase of nitriding pressure [16]. Such a process, called pressurized gas nitriding, revealed an attractive and anticipated prospect either for increasing production efficiency or for reducing energy consumption of surface treatment of the steel parts. Compared with conventional gas nitriding, the increase in nitriding pressure significantly accelerated the gas nitriding process, and promoted the rapid thickening of the nitrided layers [16]. A growing range of applications of the nitriding process, in which the layer nitrided should be characterized by better properties, required the use of intelligent control systems [17,18].

Failure of engineering materials due to corrosion, oxidation, friction, fatigue, and abrasion was undesirable on their surface. The engineering solutions to minimize or eliminate such a failure were very important. In this regard, the more commonly practiced conventional surface engineering techniques like formation of the diffusion layers, e.g., carburized or nitrided layers as well as induction surface hardened layers, possessed several limitations, like long duration, high energy and material consumption, and requirement of complex heat treatment schedule.

Laser heat treatment (LHT) was more and more often applied because of the selective hardening of parts, short hardening time, small deformation after hardening, and easy automation [19,20]. Laser surface hardening as a selective heat treatment process was usually used in surface engineering to increase the hardness of a workpiece surface [19–21]. Completely new high physical-mechanical properties of components could be achieved by the efficient formation of modified layers on the steel surface by alloying with different elements using laser heating. Laser treatment greatly increased the hardness and wear resistance of components, especially those-containing carbide, nitride, and boride phases [20,22]. Laser materials processing mainly could be carried out in three ways: without re-melting (transformation hardening), with re-melting (surface re-melting, welding, and cutting), with vaporization (cutting, drilling). The most important laser processing parameters were as follows: laser beam power or the power density of the laser beam, scanning rate, and laser beam diameter [19,20,22]. Laser beam geometry also influenced the effects of LHT [21]. The depths of modification, e.g., the

depth of re-melted zone or heat-affected zone, depended on the scanning rate and the laser beam power [22–24]. The different depths of laser modification also depended on the thermal properties of the material, and the heat penetration into the material and the rate of heat dissipation [22–24]. Some papers [24–26], presenting the models of laser heat treatment, showed the impact of laser parameters on the properties of the material processed.

In recent years, the hybrid surface treatment, consisting in the laser heat treatment of diffusion layers, was also very often applied. The nitrided layers were also laser-modified [10,27–30]. Such a treatment resulted in the improved mechanical properties of these hybrid layers [27]. The nanomechanical properties of iron nitrides (hardness and Young's modulus) produced on 42CrMo4 steel by the controlled gas nitriding and laser heat treatment with and without remelting were studied in the case of producing the multiple laser tracks [28]. The microstructure, thickness, and properties of laser-modified nitrided layers depended on the LHT parameters. The advantageous influence of LHT without remelting on the Young's modulus and hardness was confirmed for the outer ε zone as well as for the laser quenched diffusion zone [28].

In this study, the controlled gas nitriding process was followed by a laser heat treatment. The laser tracks were arranged as single laser tracks (without overlapping). The influence of the various LHT parameters, that is, the various laser beam power and scanning rate, on the microstructure of laser-modified gas-nitrided layer was studied. The temperature distribution across the laser tracks was calculated using the equations developed by Ashby and Esterling [31–33]. The calculated (based on the presented model) and measured (based on the obtained microstructure) depths of re-melted (MZ) and heat-affected (HAZ) zones were analyzed and compared. The microhardness profiles were investigated and nanomechanical properties (hardness and Young's modulus) were determined for the nitrided layer as well as the nitrided layer subjected to LHT with or without remelting.

2. Material and Methods

2.1. Material and Controlled Gas Nitriding

42CrMo4 low-alloy medium-carbon steel, containing 0.38–0.45 wt.% C, 0.9–1.2 wt.% Cr, and 0.15–0.25 wt.% Mo, was used as a base material in this study. The chemical composition of this steel was shown in the papers [28,29] in detail. The samples were prepared in the form of ring-shaped parts, having the dimensions as follows: external diameter of 20 mm, internal diameter of 12 mm, and a height of 12 mm. Such a shape of the samples resulted from the predicted wear tests in the future. Then, the laser tracks would be arranged as multiple laser tracks with an appropriate overlapping, like in the paper [30]. The specimens were austenitized at 860 °C (1123 K), quenched in oil, and then tempered at 600 °C (873 K) for 2 h.

Controlled gas nitriding in ammonia (NH_3) atmosphere was the first step of the hybrid surface treatment. The process was carried out at 570 °C (843 K) for 4 h in an atmosphere, consisting of ammonia (NH_3). The nitriding potential K_N changed during the process in order to control the microstructure of a compound zone. Therefore, the changeable flow rate of ammonia during the nitriding process was applied. This flow rate ranged from 1 to 5 L/min. Its highest value (5 L/min) was applied at the beginning. At the initial stage of gas nitriding, the nitriding potential K_N exceeded 3600 atm$^{-0.5}$. Next, the flow rate was gradually diminished in order to decrease in the nitriding potential of the atmosphere. Finally, the nitriding potential was equal to about 2 atm$^{-0.5}$ at the end of nitriding process. The full course of the nitriding potential vs. The time of nitriding was previously presented [29]. The selection of nitriding potential was very important because of its essential influence on the microstructure and thickness of compound zone. The proposed changes in K_N values resulted in the limited thickness of ε zone.

2.2. Laser Heat Treatment

The laser heat treatment (LHT) was the second stage of hybrid surface treatment. TLF 2600 Turbo CO_2 laser (TRUMPF, Poznan, Poland) of a nominal power of 2.6 kW was used during laser irradiation. The laser tracks were arranged as the single tracks without overlapping. The technique of the formation of single laser tracks was presented in Figure 1. LHT was carried out by laser irradiation of the sample, which was earlier toughened (quenched and high-temperature tempered) and gas-nitrided. The gas-nitrided layer on the surface, the toughened substrate in the core of steel as well as the single laser track produced were marked in Figure 1.
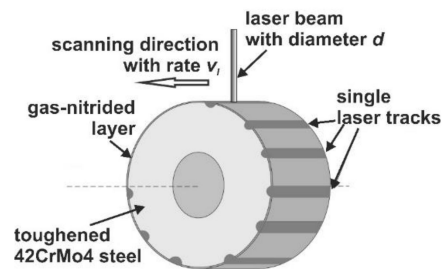
Figure 1. The technique of formation of single laser tracks.

The laser beam was moved along the cylindrical surface of the sample. The distance between the following laser tracks was selected this way that the next laser track did not influence the microstructure of the previous track. The main laser processing parameters were as follows: laser beam power (P), scanning rate (v_l), and laser beam diameter (d). The laser beam diameter (d) was constant and equal to 2 mm during all the LHT variants. The three various values of scanning rate were used: 2.24, 2.88, and 3.84 m·min^{-1}. The set, that is the designed and expected laser beam power was in the range of 0.26–0.65 kW. However, the real laser beam power often differed from the designed one. The averaging values of P, measured by the device during LHT, ranged from 0.234 to 0.624 kW. The TEM$_{01*}$ multiple mode of the laser beam was used. This special mode was a result of superposition of the two TEM$_{01}$ modes, rotated 90° with respect to one another. As a consequence, the toroidal profile of irradiance was obtained. Such an irradiance profile was advantageous because the effects of laser beam activity did not depend on the direction of laser beam movement in relation to the treated surface. The features of focusing mirror were as follows: curvature 250 mm, diameter 48 mm, and focal length 125 mm. The distance from the bottom edge of a fixing holder of focusing mirror to the laser-treated surface was equal to 106.8 mm. This distance was longer than the position of the focused beam (91.8 mm from the bottom edge of a fixing holder of the mirror).

Laser irradiation was conducted in argon shielding at a pressure of 0.2 MPa. This pressure was measured by the pressure-reducing valve installed on the cylinder with argon. High-purity argon shielding gas was supplied outside the laser beam through the same coaxial nozzle to protect the treated surface against oxidation. The laser processing parameters were shown in Table 1, providing the scanning rate (v_l), laser beam diameter (d), designed and measured laser beam power (P), and averaging irradiance (E). The averaging irradiance was calculated this way that the measured laser beam power had been divided by the circular surface of the laser beam. This important parameter usually enabled the comparison of the results of laser heat treatment, carried out with the use of various types of laser and using the various modes of the laser beam. The proposed laser processing parameters caused LHT with or without re-melting of gas-nitrided layer.

Table 1. Parameters of the laser heat treatment.

Scanning Rate v_l (m·min^{-1})	Laser Beam Diameter d (mm)	Set (Designed) Laser Beam Power P (kW)	Measured Laser Beam Power P (kW)	Averaging Irradiance E (kW/cm^2)
2.24	2	0.260	0.260	8.28
	2	0.364	0.364	11.59
2.88	2	0.260	0.234	7.45
	2	0.364	0.338	10.76
	2	0.442	0.416	13.24
	2	0.546	0.494	15.72
	2	0.598	0.624	19.86
3.84	2	0.260	0.234	7.45
	2	0.364	0.286	9.10
	2	0.442	0.390	12.41
	2	0.546	0.520	16.55
	2	0.598	0.572	18.21
	2	0.650	0.598	19.03

2.3. Microstructure Analysis and Microhardness Profiles

After the surface treatment, the samples were cut out perpendicular to the nitrided and laser-heat treated surface, across the laser tracks produced. Then, the metallographic specimens were performed. The samples were mounted in a conductive resin and polished using the abrasive paper of the different granularity, and, finally, with applying Al_2O_3 slurry. In order to reveal the microstructure, the metallographic specimens were etched using a nital reagent, i.e., 5% solution of nitric acid HNO_3 in ethanol C_2H_5OH. The cross-sectional microstructures of the nitrided and hybrid surface layers were observed using a scanning electron microscope (SEM) MIRA 3 (TESCAN, Poznan, Poland) and an optical microscope (OM) LAB-40 (OPTA-TECH, Poznan, Poland).

The microhardness was measured using the Vickers microhardness tester Micromet II (Buehler, Poznan, Poland) under a load of 50 gf (about 0.49 N) for the indentation time of 15 s. The diagonals of indentations were measured, and the Vickers hardness values were calculated. The microhardness profiles vs. The distance from the surface were determined in the nitrided layer as well as in all the hybrid surface layers (nitrided and laser heat-treated).

2.4. Modelling of the Temperature Distribution

The parameters, applied during laser heat treatment of the nitrided layer, strongly influenced the microstructure, the depths of the specific zones in this microstructure (e.g., re-melted zone or heat-affected zone), as well as the mechanical properties of the hybrid surface layer. The cycle of quick heating and cooling of the treated material caused microstructural changes in the surface area of the samples. The effect of the LHT on the microstructure of gas-nitrided layer strongly depended on the type of material, its chemical and phase composition, its physical properties, as well as the laser processing parameters used. It was obvious, that the laser re-melted zone could be formed only if the temperature close to the surface would be higher than the melting point of the treated material. Then, the re-melted zone (MZ) and heat-affected zone (HAZ) could appear in the microstructure of the produced single tracks. Such a process could be classified as the LHT with remelting. In the case of steels, if the specimen temperature reached the melting point close to the surface, the cooling rate during LHT could exceed the critical cooling rate. It resulted in the quenching process of both MZ and HAZ in which the martensite transformation proceeded. If the maximal temperature during LHT was below the melting point of the treated material, only the HAZ could be formed as a consequence of laser irradiation, and the process could be identified as the LHT without remelting. In the case of steels, the cooling rate higher than the critical cooling rate could provide the quenched HAZ with martensite.

Obviously, the presence of the nitrided layer close to the surface could significantly influence the depths of MZ and HAZ.

The equations developed by Ashby and Esterling [31–33] were adopted in order to calculate the temperature distribution vs. The distance from the surface in the axis of the single laser track. The equations used seemed to be the simple and useful tool to compare the temperature distribution during LHT using different laser processing parameters. However, some assumptions were necessary in order to simplify the calculations. The surface absorptivity A was constant and surface temperature-independent as well as depth-independent. The physical properties of the treated steel, i.e., density ρ, specific heat C_p, thermal conductivity λ, and thermal diffusivity α, were constant and temperature-independent. The initial temperature T_0 was equal to the ambient temperature of 20 °C (293 K) and was constant during the laser treatment. The laser beam was moved in the x-direction with the scanning rate v_l.

According to the papers [31–34], when the laser beam with a power P and radius r_B was moved in the scanning direction x with rate v_l, each point below the center of a single laser track for $y = 0$ attained the temperature $T(z, t)$, well approximated according to the equation:

$$T(z,\ t) = T_0 + \frac{AP}{2\pi\lambda v_l[t(t+t_0)]^{\frac{1}{2}}} \times \exp\left\{-\left(\frac{(z+z_0)^2}{4\alpha t}\right)\right\} \tag{1}$$

where, $T(z, t)$ is the temperature (K) below the center of laser track at the depth z, z is the depth below the center of laser track (m), T_0 is the initial (ambient) temperature (K), A is the absorptivity at the sample surface, P is the laser beam power (W), λ is the thermal conductivity of material (W·m^{-1}·K^{-1}), v_l is the scanning rate of laser beam (m·s^{-1}), t is the interaction time (s), t_0 is the time constant (s), z_0 is the depth constant (m), α is the thermal diffusivity of material (m^2·s^{-1}).

Thermal diffusivity α could be calculated using the equation:

$$\alpha = \frac{\lambda}{\rho C_p} \tag{2}$$

where, λ is the thermal conductivity of material (W·m^{-1}·K^{-1}), ρ is the density of material (kg·m^3), C_p is the specific heat of material (J·kg^{-1}·K^{-1}).

The time constant t_0 was defined as a time required for heat diffusion over a distance equal to the laser beam radius r_B:

$$t_0 = \frac{r_B^2}{4\alpha} \tag{3}$$

where, r_B is the laser beam radius (m), α is the thermal diffusivity of material (m^2·s^{-1}).

The depth constant z_0 corresponded to the distance from the surface over which heat could diffuse during the interaction time of a laser beam. The interaction time could be calculated as a ratio of the laser beam radius to the scanning rate r_B/v_l. Depending on the relation between interaction time t and the time constant t_0, the two equations could be used for calculation of the depth constant z_0. If $t \gg t_0$, the depth constant z_0 could be calculated using the equation:

$$z_0^2 = \left[\frac{r_B}{e} \cdot \left(\frac{\pi\alpha r_B}{v_l}\right)^{\frac{1}{2}}\right] \tag{4}$$

where, r_B is the laser beam radius (m), e is the base of natural logarithms, α is the thermal diffusivity of material (m^2·s^{-1}), v_l is the scanning rate of laser beam (m·s^{-1}).

If $t \ll t_0$, the constant z_0 can be expressed by the equation:

$$z_0^2 = \frac{\pi\alpha r_B}{2ev_l} \tag{5}$$

where, r_B is the laser beam radius (m), e is the base of natural logarithms, α is the thermal diffusivity of material (m^2·s^{-1}), v_l is the scanning rate of laser beam (m·s^{-1}).

The relation between time constant t_0 and interaction time t determined the selection of an equation used for calculation of depth constant z_0. The value of time constant t_0 depended only on the laser beam radius r_B and the thermal diffusivity of treated material α. In the present study laser beam diameter was constant (d = 2 mm). For this reason, the time constant t_0 was the same for all the considered laser processing parameters. On the contrary, the interaction time t was related to the scanning rate v_l. Therefore, the value of t differed depending on scanning rate v_l. The calculated values of time constant t_0 and interaction time t were presented in Table 2. In the case of the lowest scanning rate of 2.24 m·min^{-1} the interaction time t was higher than the time constant t_0. In these two cases, the depth constant z_0 was calculated according to the Equation (4). In the case of higher scanning rates (2.88 and 3.84 m·min^{-1}), the interaction time t was lower than the time constant t_0. Therefore, in these cases, Equation (5) was used for z_0 calculation.

Table 2. Influence of laser heat treatment parameters on time constant t_0 and interaction time t.

Scanning Rate v_l (m·min^{-1})	Measured Laser Beam Power P (kW)	Time Constant t_0 (s)	Interaction Time t (s)	t to t_0 Relation
2.24	0.260	0.0221	0.02679	$t \gg t_0$
	0.364	0.0221	0.02679	$t \gg t_0$
2.88	0.234	0.0221	0.02083	$t \ll t_0$
	0.338	0.0221	0.02083	$t \ll t_0$
	0.416	0.0221	0.02083	$t \ll t_0$
	0.494	0.0221	0.02083	$t \ll t_0$
	0.624	0.0221	0.02083	$t \ll t_0$
3.84	0.234	0.0221	0.01563	$t \ll t_0$
	0.286	0.0221	0.01563	$t \ll t_0$
	0.390	0.0221	0.01563	$t \ll t_0$
	0.520	0.0221	0.01563	$t \ll t_0$
	0.572	0.0221	0.01563	$t \ll t_0$
	0.598	0.0221	0.01563	$t \ll t_0$

The physical properties of the 42CrMo4 steel, used as the laser heat-treated substrate were assumed as follows [35]: material density ρ = 7850 (kg·m^{-3}), thermal conductivity λ = 42 (W·m^{-1}·K^{-1}), and specific heat of material C_p = 473 (J·kg^{-1}·K^{-1}). Hence, the thermal diffusivity α was equal to 1.131×10^{-5} (m^2·s^{-1}) according to Equation (2).

2.5. Nanomechanical Testing

The nanomechanical properties (hardness and Young's modulus) were investigated using nanoindentation tester NHT^2 (Anton Paar, Poznan, Poland) equipped with a Berkovich diamond tip. The ability to measure the penetration depth of indenter under the applied load was an important feature of nanoindentation. It was possible to measure both the plastic and elastic deformations of the tested material. The contact depth could be determined based on the analysis of the indentation curve (load-displacement curve) during loading and unloading. The maximal load F_{max} was equal to 50 mN. The device enabled the recording of the penetration depth and load vs. time as well as the load-displacement curves (load vs., penetration depth). The measurements of nanomechanial properties were conducted based on Oliver and Pharr's theory [36]. The values of indentation hardness H_{IT}, Vickers hardness HV_{IT}, reduced modulus E_r, plane-strain modulus E^* as well as the indentation modulus E_{IT} were calculated according to the equations which were reported in the paper [28].

The appropriate values of Poisson's ratio (ν_s) should be accepted in order to calculate indentation moduli (E_{IT}). Poisson's ratio strongly depends on the material microstructure, i.e., the phase measured.

Poisson's ratios of ε (Fe$_{2\text{-}3}$N) and γ' (Fe$_4$N) iron nitrides, reported by literature data [37–46], were analyzed in the paper [28] in detail. Based on this analysis, the following Poisson's ratios were taken into account for the calculations: $\nu_s = 0.3029$ for ε (Fe$_{2\text{-}3}$N) phase, and $\nu_s = 0.3532$ for γ' (Fe$_4$N) phase. However, the measurements in the $\varepsilon + \gamma'$ zone required to accept the averaging value of Poisson's ratio taking its values for both phases (ε and γ') into consideration. Hence, the Poisson's ratio $\nu_s = 0.3281$ was accepted for $\varepsilon + \gamma'$ zone. The same values of ν_s were used in the previous paper [28]. The standard value of Poisson's ratio $\nu_s = 0.3$ was accepted for the other zones, i.e., diffusion zone, re-melted zone, heat-affected zone, and substrate material.

3. Results and Discussion

3.1. Microstructure Characterization

Figure 2 shows the SEM images of microstructure of 42CrMo4 steel after the controlled gas nitriding at 570 °C for 4 h. As usual, before gas nitriding, the substrate material (42CrMo4 steel) was subjected to quenching and high-temperature tempering, i.e., to toughening. After such a heat treatment, the microstructure of base material consisted of the sorbite, i.e., the mixture of ferrite and cementite, produced as a consequence of the diffusion transformation of martensite during tempering. Next, this steel was gas-nitrided. The diffusion process resulted in the saturation of the surface with nitrogen. Nitriding potential was gradually diminished in order to limit the thickness of the porous ε phase. However, the presence of porous ε nitrides close to the surface was advisable in order to check the effect of laser irradiation on the microstructure of this phase. The selected parameters of gas nitriding facilitated the rapid formation of a compound zone with limited thickness close to the surface. Simultaneously, the nitriding potential was higher than the boundary potential between the γ' and ε phases according to the Lehrer diagram, the value of which slightly exceeded 1 atm$^{-0.5}$ at the temperature applied [3]. After the process, the nitrogen concentration obtained a maximal value close to the surface, diminishing towards the core of steel.
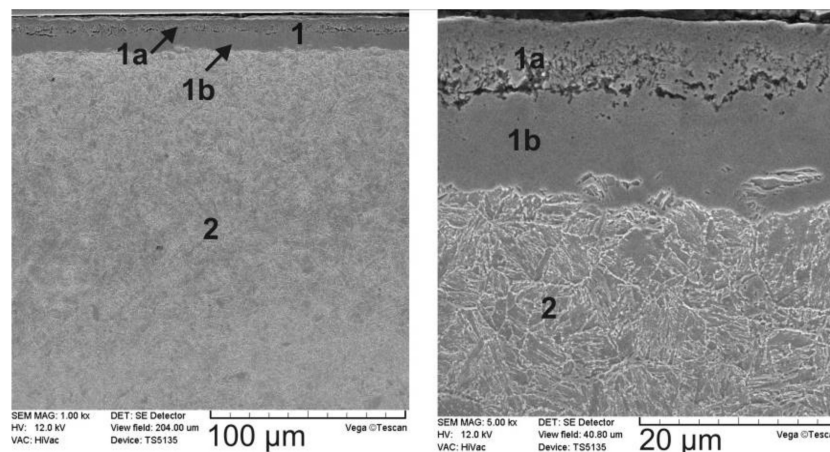
Figure 2. SEM images of gas-nitrided layer produced on 42CrMo4 steel: 1—compound zone; 1a—zone with ε nitrides; 1b—zone with $\varepsilon + \gamma'$ nitrides; 2—diffusion zone (nitric sorbite with γ' precipitates).

As a consequence of controlled gas nitriding, the nitrided layer consisted of a compound zone (1) and a diffusion zone (2). The two regions were clearly visible in the compound zone (see the right SEM image in Figure 2). A porous ε nitrides (zone 1a) were observed close to the surface. Below this region, more compact zone 1b with $\varepsilon + \gamma'$ nitrides was observed. The averaging thickness of the whole compound zone, i.e., $\varepsilon + (\varepsilon + \gamma')$ nitrides, was equal to 19.35 μm. The phase analysis by XRD confirmed the presence of both ε and γ' phases in a compound zone in the case of the similar nitrided layer [28,29]. In the diffusion zone (2), the nitric sorbite with precipitates of γ' nitrides occurred. The total thickness

of the produced nitrided layer was equal to about 450 µm based on the microstructure observation. Below the diffusion zone, the microstructure resulted from the heat treatment, carried out before nitriding. It was typical of a quenched and high-temperature tempered base material, and consisted of sorbite. The microstructure of this zone was invisible in Figure 2.

The OM microstructure of the single laser tracks, produced by hybrid surface treatment (gas nitriding + LHT) at various scanning rates 2.24, 2.88, and 3.84 m·min^{-1}, is shown in Figure 3. Laser processing was carried out with or without re-melting. It depended on LHT parameters, which modified the microstructure of nitrided layer. If the scanning rate was equal to 2.24 m·min^{-1} (see Figure 3a), only the two laser beam powers were used (0.260 and 0.364 kW). The laser beam power of 0.260 kW resulted in the presence of the partially re-melted compound zone (1a) and heat-affected zone (2). An amount of iron nitrides was still visible in the compound zone after LHT. Only the porous ε nitrides, occurring close to the surface, were partially re-melted (zone 1a). Due to the relatively high cooling rate, exceeding the critical cooling rate, the martensite transformation proceeded in the HAZ. Hence, the fine-grained nitric martensite was formed in this zone. During the heating, nitrogen partially dissolved in the austenite and remained in the produced martensite. However, an amount of γ' precipitates could remain in HAZ. Below the HAZ, the diffusion zone without visible effects of laser modification (3) occurred. Its microstructure consisted of nitric sorbite with precipitates of γ' phase. After laser modification with the use of the higher laser beam power (0.364 kW), the microstructure was typical of the laser remelting. The three zones were observed in the microstructure of hybrid surface layer: re-melted zone (1), heat-affected zone (2), and nitrided layer (precisely its diffusion zone) without visible effects of LHT (3). The microstructure of MZ, HAZ, and the diffusion zone without visible effects of LHT consisted of coarse-grained nitric martensite with possible ε precipitates [27], fine-grained nitric martensite with γ' precipitates, and nitric sorbite with γ' precipitates, respectively. The increase in the laser beam power caused the increased dimensions of laser track, i.e., increased depths and widths of MZ and HAZ.

Figure 3b shows the OM microstructure of the single laser tracks, produced using the scanning rate v_l = 2.88 m·min^{-1}. The laser beam power (*P*) ranged from 0.234 to 0.624 kW. The use of a relatively low laser beam power (0.234 and 0.338 kW) resulted in the formation of the partially re-melted compound zone (1a) and heat-affected zone (2). Whereas the laser beam power in the range of 0.416 to 0.624 kW caused the microstructure of the laser tracks to consist of re-melted zone (1) and heat-affected zone (2). An amount of iron nitrides remained in the compound zone after LHT and was still visible in the partially re-melted compound zone (1a). However, if the laser beam power was equal to 0.234 kW, the continuous $\varepsilon + \gamma'$ zone remained after LHT. The use of the laser beam power of 0.338 kW resulted in the formation of the discontinuous iron nitrides in partially re-melted zone (1a). In the microstructure of MZ (1), the coarse-grained nitric martensite with possible ε precipitates [27] appeared, whereas the fine-grained nitric martensite with γ' precipitates always occurred in the HAZ (2). Below the heat-affected zone (2), the diffusion zone without visible effects of LHT (3) was visible. Its microstructure, like previously, consisted of nitric sorbite with γ' precipitates. The dimensions of laser tracks (i.e., the depths and widths of MZ and HAZ) were greater if the laser beam power increased.

The OM microstructure of laser tracks, formed at a scanning rate of 3.84 m·min^{-1}, is presented in Figure 3c. The laser beam power (*P*) was used in the range of 0.234–0.598 kW. In this case, the more variants of microstructure were observed. The use of the lowest laser beam power *P* = 0.234 kW resulted in the presence of the compound zone without visible effects of remelting (1b) and heat-affected zone (2). It seemed that the $\varepsilon + (\varepsilon + \gamma')$ compound zone remained in the microstructure and the laser irradiation caused only the formation of the HAZ, i.e., the partial hardening of the diffusion zone due to the presence of a fine-grained nitric martensite with γ' precipitates. The second laser beam power (*P* = 0.286 kW) caused the formation of the zones as follows: the partially re-melted compound zone (1a) and heat-affected zone (2). An amount of iron nitrides, especially the continuous $\varepsilon + \gamma'$ zone, remained in the compound zone after LHT and was still visible close to the surface. Finally, the laser beam power in the range of 0.390–0.598 kW caused the formation of the microstructure consisting of

re-melted zone (1) and heat-affected zone (2). The diffusion zone without visible effects of LHT (3) was visible below the heat-affected zone in all the cases. This zone consisted of nitric sorbite with γ' precipitates. Like previously, the dimensions of laser tracks (i.e., the depths and widths of MZ and HAZ) increased if the laser beam power was higher. The typical sorbite was characteristic of the microstructure of the base material (quenched and high-temperature tempered 42CrMo4 steel). In all the produced laser tracks, it was easy to identify and measure the depths of partially re-melted compound zones (1a), compound zones without visible effects of remelting (1b), re-melted zones (1), and heat-affected zones (2). In general, the higher scanning rate, the smaller size of laser tracks at the same laser beam power.
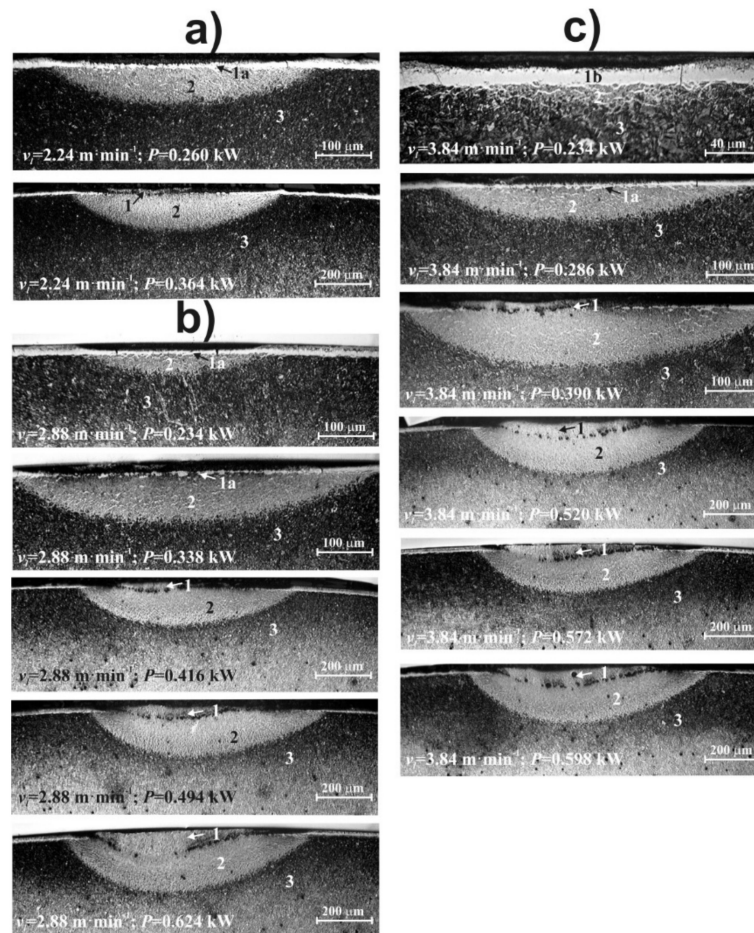
Figure 3. OM images of single laser tracks produced on gas-nitrided 42CrMo4 steel using a scanning rate of 2.24 m·min^{-1} (**a**); 2.88 m·min^{-1} (**b**); and 3.84 m·min^{-1} (**c**); 1—re-melted zone (MZ), 1a—partially re-melted compound zone, 1b—compound zone without visible effects of remelting, 2—heat-affected zone (HAZ), 3—nitrided layer without visible effects of LHT (diffusion zone).

The microstructures of the two-laser track, produced after gas nitriding with and without remelting, were compared taking into account the distribution of iron and nitrogen, measured by Energy Disspersive X-ray Spectroscopy (EDS). SEM images and EDS patterns of iron and nitrogen are shown in Figure 4. In the case of LHT without remelting (Figure 4a), it is clearly visible that the increased concentration of nitrogen remained in $\varepsilon + (\varepsilon + \gamma')$ compound zone (1), which was not re-melted. Whereas in the HAZ (2), the change in nitrogen concentration was invisible. Simultaneously, the slightly increased iron concentration was observed in the compound zone (1) as well as heat-affected zone (2). The area of laser activity is characterized in Figure 4a by the width and depth of HAZ (w_{HAZ} and d_{HAZ}, respectively). In the upper part of this figure, the gas-nitrided layer without the

laser irradiation was visible (zones: 1N and 3N). The EDS patterns in this area did not differ from those-obtained in the region, which was laser heat-treated without remelting. After the LHT with remelting (Figure 4b), the iron nitrides were re-melted and nitrogen dissolved in the MZ (1), in which the slightly increased concentration of this element appeared. However, an amount of ε phase could remain in this zone [27] because of the short time of heating. Simultaneously, the slightly increased concentration of iron was visible in MZ (1) and HAZ (2), probably as a consequence of martensite transformation in these zones.
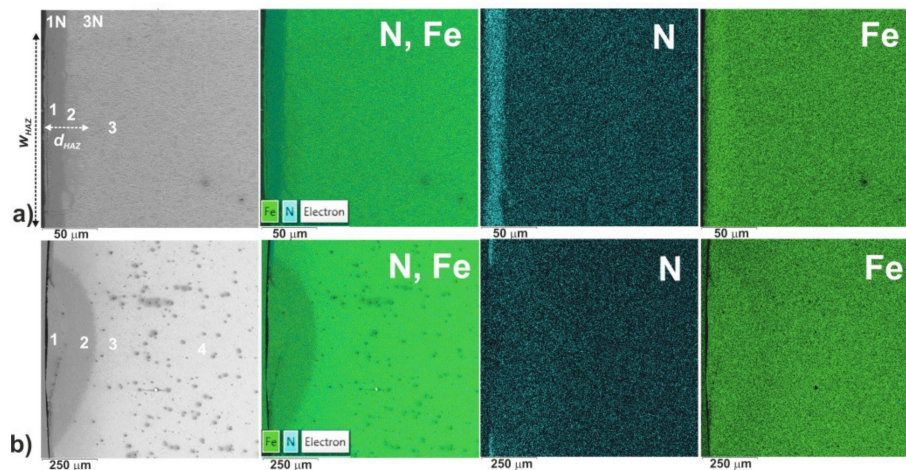
Figure 4. SEM images of single laser tracks and corresponding EDS patterns of iron and nitrogen after gas nitriding and LHT: without remelting using P = 0.234 kW and v_l = 3.84 m·min^{-1} (**a**) and with remelting using P = 0.624 kW and v_l = 2.88 m·min^{-1} (**b**); 1—compound zone without visible effects of remelting (**a**) or MZ (**b**); 2—HAZ, 3—nitrided layer without visible effects of LHT (diffusion zone), 4—substrate material, 1N—compound zone of nitrided layer, 3N—diffusion zone of nitrided layer.
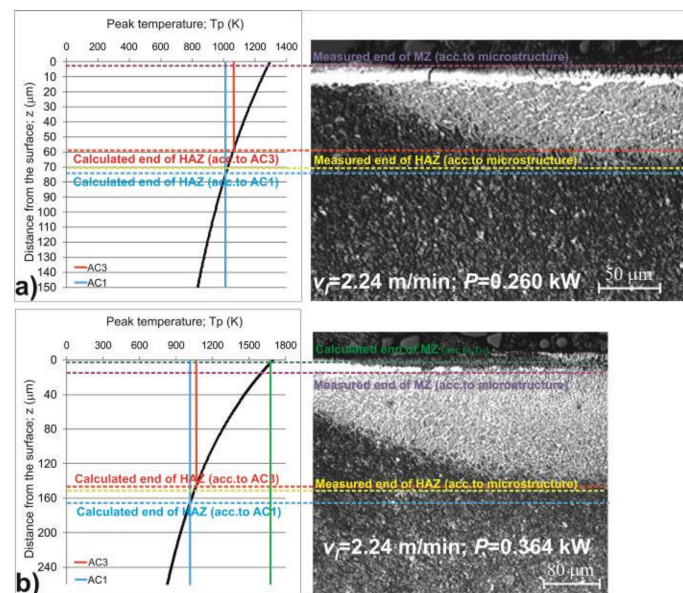
3.2. Effect of the Temperature Distribution on the Microstructure of Laser Tracks

The temperature distribution during laser heat treatment depended on the laser processing parameters (laser beam radius r_B, laser beam power P, scanning rate v_l) as well as the physical properties of the treated material (density ρ, specific heat C_p, thermal conductivity λ, thermal diffusivity α). In the present study, the gas nitrided 42CrMo4 steel was subjected to laser modification using the different parameters (see Table 1). Therefore, some differences were expected in the effect of LHT, e.g., in the surface temperature and temperature distribution vs., the distance from the surface. The temperature distribution influenced the microstructure, the depths of re-melted zone (MZ), and heat-affected zone (HAZ) as well as the hardness of laser-modified nitrided layer. In order to determine the depths of re-melted zone and heat-affected zone, the melting point and austenitizing temperature were needed. In order to determine the depths of MZ (d_{MZ}) and HAZ (d_{HAZ}), the characteristic temperatures of the treated material were needed, i.e., its melting point T_m, eutectoid temperature *AC1* and temperature of allotropic transformation *AC3*. The *AC1* and *AC3* temperatures of 42CrMo4 steel were equal to 1018 K (745 °C) and 1063 K (790 °C), respectively. They were assumed based on the technical card of Lucefin Group [47]. According to the data of Xingsheng Special Steel company [48], the melting point T_m of 42CrMo4 was equal to 1689 K (1416 °C). Such temperatures were taken into account in order to calculate the d_{MZ} and d_{HAZ} values based on the temperature distribution vs. The distance from the surface.

It was assumed that the end of MZ (d_{MZ}) should correspond to the melting point T_m. Simultaneously, the end of HAZ (d_{HAZ}) was expected at the depth, which should be between the two depths related to *AC3* and *AC1* temperatures, respectively. Such assumptions resulted from the unquestionable fact that the re-melted zone should occur between the depth equal 0 (corresponding to the maximal temperature at the surface) and the depth corresponding to the melting point T_m if,

obviously, the maximal temperature would be higher than T_m. Then, the LHT with remelting would be carried out. The HAZ would appear between the depth related to T_m and the depth related to *AC3* or *AC1* temperature. If *AC3* was the limiting temperature of this zone, the microstructure of HAZ would consist of the martensite mainly. While, if *AC1* temperature was accepted as limiting temperature, the mixture of martensite and ferrite would appear at the end of HAZ. If the maximal temperature was lower than T_m, the MZ would not appear. It would correspond to the LHT without remelting. Then, the $\varepsilon + (\varepsilon + \gamma')$ compound zone would remain in the microstructure. Below the iron nitrides, the HAZ would be observed up to depth related to *AC3* or *AC1* temperature.

The temperature distribution $T(z, t)$ along the axis of a single laser track was calculated as a function of the distance from the surface. The results were shown as a graph, related to the obtained microstructure for each variant of LHT parameters used. Figures 5–7 show these results for the scanning rates 2.24, 2.88, and 3.84 m·min^{-1}, respectively. The melting point T_m, eutectoid temperature *AC1* and temperature of allotropic transformation *AC3* are marked in the presented diagrams of temperature distribution together with calculated depths of MZ (d_{MZ}) and HAZ (d_{HAZ}). Simultaneously, the measured values of d_{MZ} and d_{HAZ} are shown based on the microstructure observations.
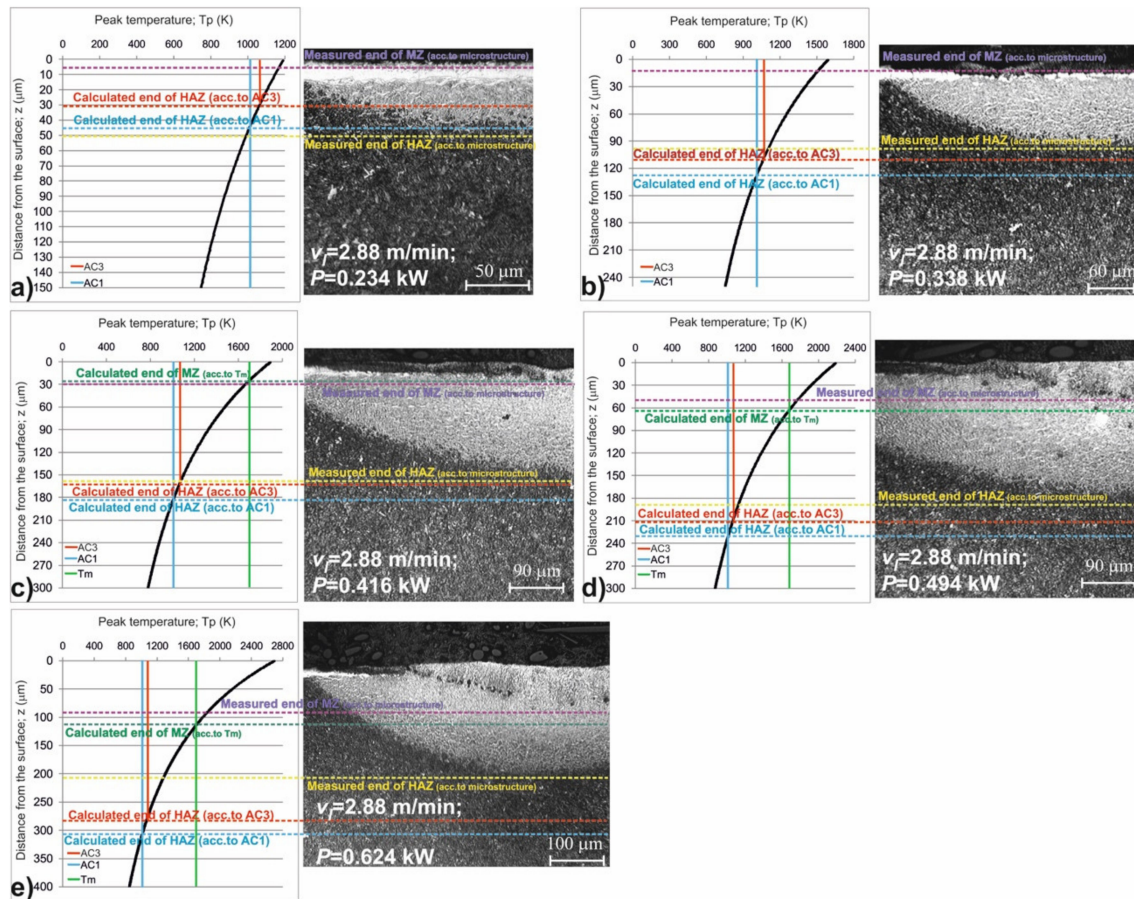

Figure 5. Temperature distribution along the axes of laser tracks and related microstructures after laser modification of gas-nitrided layer using scanning rate $v_l = 2.24$ m·min^{-1} and $P = 0.260$ kW (**a**) or $P = 0.364$ kW (**b**).

In Figure 5, the temperature distribution along the axes of laser tracks and related microstructures are shown for gas-nitrided 42CrMo4 steel after laser heat treatment using the scanning rate $v_l = 2.24$ m·min^{-1} and the two laser beam powers (0.260 and 0.364 kW). The maximal temperature, obtained at the surface (1294 K) at laser beam power $P = 0.260$ kW, was lower than melting point of the substrate material (Figure 5a). Therefore, the laser beam action should not cause remelting. However, based on the microstructure observation, the compound zone was slightly re-melted up to a depth of 3 µm (measured end of MZ). The temperature along the axis of a laser track gradually decreased with an increase in the distance from the surface. The measured end of HAZ, i.e., depth of this zone d_{HAZ} (related to microstructure), was equal to 71 µm. This value ranged between the depths of HAZ related to *AC3* and *AC1* temperatures (59 and 74 µm, respectively) and calculated using the temperature distribution. The use of the second laser beam power $P = 0.364$ kW (Figure 5b) resulted close to the surface in the maximal temperature of 1693 K, which was slightly higher than melting point of the substrate (1689 K). Hence, the calculated end of MZ, i.e., depth of this zone d_{MZ}, was equal to 2 µm

based on the temperature distribution. However, the measured value of d_{MZ} (related to microstructure) was higher, obtaining 15 μm, and the re-melted zone was clearly visible. Like previously, the measured end of HAZ (d_{HAZ} = 151 μm) ranged between the values related to *AC3* and *AC1* temperatures (147 and 164 μm, respectively) according to the temperature distribution.

Figure 6. Temperature distribution along the axes of laser tracks and related microstructures after laser modification of gas-nitrided layer using scanning rate v_l = 2.88 m·min^{-1} and laser beam power as follows: *P* = 0.234 kW (**a**); *P* = 0.338 kW (**b**); *P* = 0.416 kW (**c**); *P* = 0.494 kW (**d**); and *P* = 0.624 kW (**e**).

The temperature distribution along the axes of laser tracks and related microstructures are shown in Figure 6 for gas-nitrided 42CrMo4 steel after laser heat treatment using the scanning rate v_l = 2.88 m·min^{-1} and the laser beam powers in the range of 0.234–0.624 kW. At laser beam power of 0.234 kW, the maximal temperature close to the surface (1192 K) was lower than melting point of the substrate material (Figure 6a). Hence, the laser irradiation should not form the MZ. However, the microstructure observation indicated that the compound zone was slightly re-melted up to a depth of 5 μm (measured end of MZ). The gradual decrease in the temperature along the axis of this laser track was observed with an increase in the distance from the surface. The measured end of HAZ (related to microstructure), i.e., depth of this zone d_{HAZ}, was equal to 51 μm. The measured d_{HAZ} was outside the depth range (31–43 μm) determined by the depths of HAZ related to *AC3* and *AC1* temperatures (based on the temperature distribution), obtaining the slightly higher value. The next laser beam power *P* = 0.338 kW used (Figure 6b) also resulted in the lower maximal temperature (1592 K) than melting point of the substrate (1689 K). In this case, the MZ should not be formed. However, the compound zone was partially re-melted, and the measured value of d_{MZ} (related to microstructure) was equal to 13 μm. Like previously, the measured end of HAZ (d_{HAZ} = 100 μm) was outside the depth range

related to *AC3* and *AC1* temperatures (111–126 μm) according to the temperature distribution. In this case, the measured d_{HAZ} was slightly lower. The use of the next laser beam power (*P* = 0.416 kW) resulted in the maximal temperature of 1892 K, which was clearly higher than melting point of the substrate (1689 K). The temperature distribution, related to the microstructure, is shown in Figure 6c. It caused the compound zone to re-melt. The calculated and measured depths of MZ were similar, obtaining the values of 27 and 30 μm, respectively. The measured depth of HAZ (d_{HAZ} = 151 μm) was slightly lower than its depth range (164–180 μm) related to *AC3* and *AC1* temperatures.
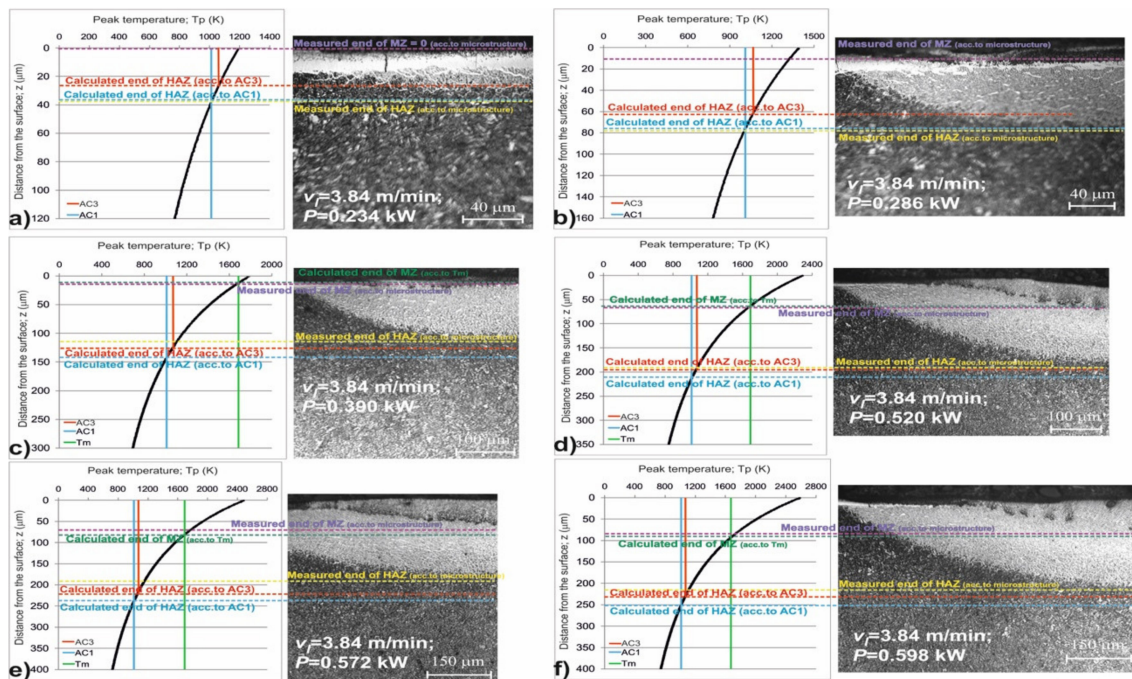
Figure 7. Temperature distribution along the axes of laser tracks and related microstructures after laser modification of gas-nitrided layer using scanning rate v_l = 3.84 m·min^{-1} and laser beam power as follows: *P* = 0.234 kW (**a**); *P* = 0.286 kW (**b**); *P* = 0.390 kW (**c**); *P* = 0.520 kW (**d**); *P* = 0.572 kW; (**e**) and *P* = 0.598 kW (**f**).

The re-melted zone was also visible after LHT using the laser beam power of 0.494 kW. The effect of temperature distribution on the microstructure was shown in Figure 6d. The maximal temperature (2191 K) significantly exceeded the melting point of the substrate (1689 K). The depths of MZ, measured based on microstructure observation and calculated based on temperature distribution, slightly differed, obtaining the values of 49 and 63 μm, respectively. Whereas the measured depth of HAZ (d_{HAZ} = 188 μm) was clearly outside the depth range (212–230 μm), calculated for *AC3* and *AC1* temperatures. Larger differences between calculated and measured depths of MZ and HAZ were observed after LHT using the laser beam power of 0.624 kW (Figure 6e). The maximal temperature close to the surface was equal to 2691 K. The measured depth of MZ (d_{MZ} = 90 μm) was significantly lower than the value calculated for the melting point (d_{MZ} = 116 μm). The measured depth of HAZ (d_{HAZ} = 207 μm) was even more outside the depth range (284–304 μm), related to *AC3* and *AC1* temperatures.
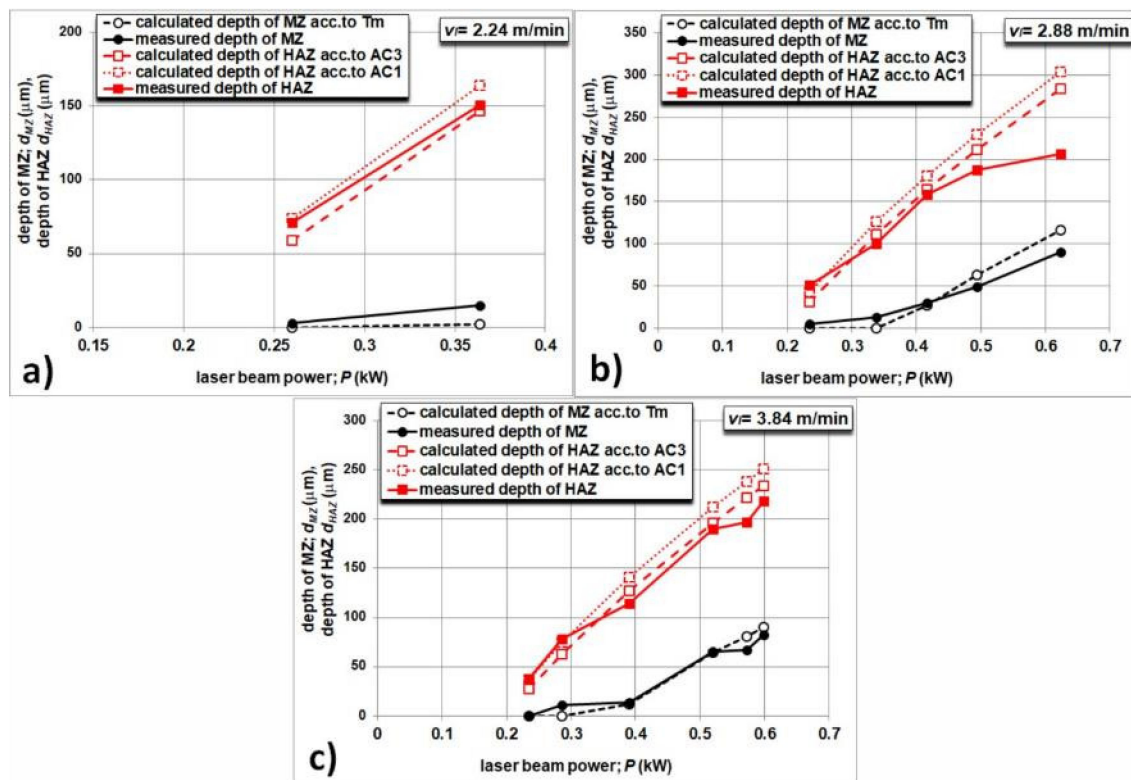
In Figure 7, the temperature distribution along the axes of laser tracks and related microstructures are shown for gas-nitrided 42CrMo4 steel after LHT using the scanning rate v_l = 3.84 m·min^{-1} and the laser beam power in the range of 0.234–0.598 kW. At laser beam power of 0.234 kW, the maximal temperature close to the surface (1192 K) was significantly lower than melting point of the substrate material (Figure 7a). The calculated and measured depths of MZ (d_{MZ}) were the same, obtaining the value of 0 μm. It was indicated that the laser heat treatment without remelting was observed. The ε

+ (ε + γ′) compound zone remained after LHT. It was the only case during the laser modification of gas-nitrided layer. The measured depth of HAZ (d_{HAZ} = 38 μm), based on the microstructure observation, was slightly higher than its depth range (27–37 μm) related to *AC3* and *AC1* temperatures. Although the maximal temperature at the surface (1391 K) was lower than the melting point of the substrate, the laser beam power of 0.286 kW resulted in the formation of the partially re-melted compound zone (Figure 7b). The measured depth of MZ (based on microstructure observation) was equal to 11 μm. Like in the previous case, the measured depth of HAZ (d_{HAZ} = 78 μm), based on the microstructure observation, was slightly higher than its depth range (63–75 μm) related to *AC3* and *AC1* temperatures and calculated using the temperature distribution. The LHT using the laser beam power *P* = 0.390 kW (Figure 7c) caused the formation of re-melted zone (MZ) and heat-affected zone (HAZ) due to the relatively high maximal temperature (1791 K), which exceeded the melting point of the substrate (1689 K). The calculated and measured values of d_{MZ} were similar, obtaining 12 and 14 μm, respectively. Whereas the measured depth of HAZ (d_{HAZ} = 114 μm) was outside the depth range (127–142 μm), calculated for *AC3* and *AC1* temperatures.

The next laser beam power (0.520 kW) resulted in the still higher maximal temperature (2290 K). Hence, the depths of MZ and HAZ were even greater (Figure 7d). The calculated and measured depths of MZ (d_{MZ}) were almost the same (64 and 65 μm, respectively). Like previously, the measured depth of HAZ (d_{HAZ}) was outside the depth range (196–212 μm), determined for *AC3* and *AC1* temperatures. Its value was slightly smaller (190 μm) than the lower limit of this range. The next laser beam powers (0.572 and 0.598 kW) caused still deeper remelting because the maximal temperatures (2489 and 2589 K, respectively) significantly exceeded the melting point (1689 K). In general the depths of MZ and HAZ were greater with the increase in laser beam power (Figure 7e,f). In the case of *P* = 0.572 kW (Figure 7e), the measured depth of MZ (d_{MZ}) was equal to 67 μm, being slightly smaller than the calculated value (81 μm), whereas, the measured depth of HAZ (d_{HAZ} = 197 μm) was outside the depth range (222–238 μm), calculated for *AC3* and *AC1* temperatures. The use of the laser beam power of 0.598 kW (Figure 7f) resulted in the slightly smaller measured depth of MZ (d_{MZ} = 82 μm) than the calculated value (90 μm). Like previously, the measured depth of HAZ (d_{HAZ} = 218 μm) was smaller than the lower limit of the depth range (234–251 μm), which was determined by *AC1* and *AC3* temperatures.

In Figure 8, the calculated and measured values of d_{MZ} and d_{HAZ} are compared for all the applied laser processing parameters. Only the two laser beam powers were used during LHT at scanning rate v_l = 2.24 m·min^{-1} (Figure 8a). The laser beam power of 0.260 kW should not cause remelting of the compound zone. However, the iron nitrides were partially re-melted. The measured and calculated depths of MZ differed slightly. Whereas the measured depths of HAZ were in the depth range, determined by *AC3* and *AC1* temperatures. At scanning rate v_l = 2.88 m·min^{-1} (Figure 8b), the measured depths of MZ were initially slightly greater than the calculated values. Such a situation was observed if the laser beam power did not exceed 0.416 kW. The next laser beam powers resulted in the diminished measured values of d_{MZ} when compared to the calculated depths. Up to the laser beam power of 0.494 kW, the measured depths of HAZ slightly differed from the calculated values, being outside the depth range determined by *AC3* and *AC1* temperatures. The significant difference was observed if the laser beam power of 0.624 kW was used. In general, at a scanning rate v_l = 3.84 m·min^{-1} (Figure 8c), the measured depths of MZ and HAZ were close to the calculated values. Only the laser beam higher than 0.520 kW resulted in larger differences. The diagrams, presented in Figure 8, showed that the depths of re-melted zone and heat-affected zone could be efficiently predicted using the equations developed by Ashby and Esterling [31–33]. The accuracy of this prediction could be better if some of the physical properties of iron nitrides, such as thermal conductivity λ and specific heat of material C_p, were known. However, there were no data in the literature regarding these properties.

Figure 8. The effect of laser beam power on the measured and calculated depths of MZ (d_{MZ}) and HAZ (d_{HAZ}) at scanning rate of: 2.24 m·min^{-1} (**a**); 2.88 m·min^{-1} (**b**); and 3.84 m·min^{-1} (**c**).

3.3. Effect of the Temperature Distribution on Microhardness Profiles

The microhardness profiles along the axes of the produced single laser tracks after gas nitriding are presented in Figures 9–11. The measurements were carried out perpendicular to the treated surface and compared to the microhardness profile after the controlled gas nitriding. The maximal hardness of the gas-nitrided 42CrMo4 steel was measured in compound zone and was equal to 759.4 HV. Next, the gradual decrease in microhardness was observed. In the diffusion zone, the microhardness decreased from 654.8 (close to the compound zone) to 346.8 HV at the end of diffusion zone. The end of the diffusion zone, assumed as the depth at which the hardness obtained the values characteristic of the substrate, corresponded to about 450 μm. The toughened (quenched and high-temperature tempered) substrate material had a hardness of about 320–340 HV. As a consequence of the various laser processing parameters (scanning rate and laser beam power), the LHT was carried with complete remelting of the compound zone, with partial remelting of compound zone or without remelting. The temperature distribution during LHT influenced the microstructure produced. It resulted in the different microhardness profiles along the laser tracks. In general, the changes in microstructure, especially the appearance of nitric martensite in MZ and in HAZ, could result in the increased microhardness.

The microhardness profiles of single laser tracks, produced in the gas-nitrided 42CrMo4 steel at scanning rate v_l = 2.24 m·min^{-1} and the two laser beam powers used (0.260 and 0.364 kW), are shown in Figure 9. The use of P = 0.260 kW resulted in the formation of very thin partially re-melted compound zone and heat-affected zone. It was difficult to measure the microhardness of partially re-melted zone because of its small depth. The microhardness of HAZ ranged from 732.6 to 833 HV and was significantly increased when compared to the same area of diffusion zone in gas-nitrided layer. The hardening of this zone occurred as a consequence of martensite transformation. Below the HAZ, the microhardness profile was characteristic of the rest part of diffusion zone, which was

not subjected to LHT. Laser beam power of 0.364 kW caused the formation of clearly visible MZ (completely re-melted compound zone) and HAZ. The microhardness of re-melted compound zone (MZ) was equal to 698 HV and was slightly lower than the microhardness of the iron nitrides before LHT. The HAZ was characterized by the microhardness in the range of 726.1–916 HV. Its maximal value exceeded the microhardness, usually obtained after typical quenching of 42CrMo4 steel (about 700–750 HV). It resulted from the increased hardenability due to the formation of austenite enriched in nitrogen before the martensite transformation. Hence, the martensite, supersaturated with carbon, additionally contained nitrogen. Besides, an amount of γ′ precipitates could remain in HAZ and also cause the increase in hardness. The microhardness of MZ was lower than that of HAZ because of the presence of coarse-grained nitric martensite, whereas in HAZ, the fine-grained martensite occurred.
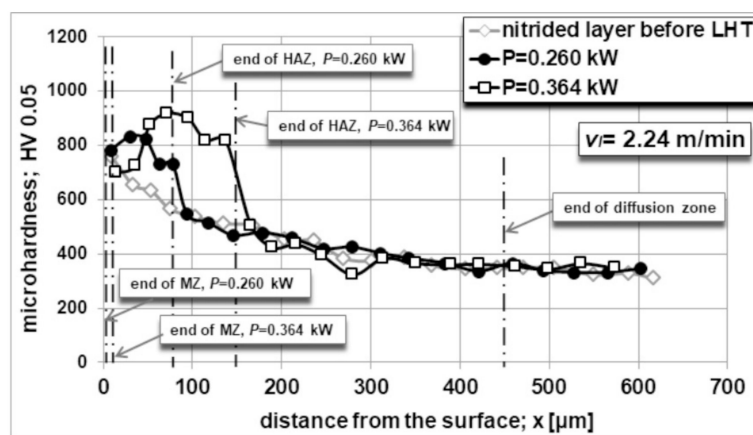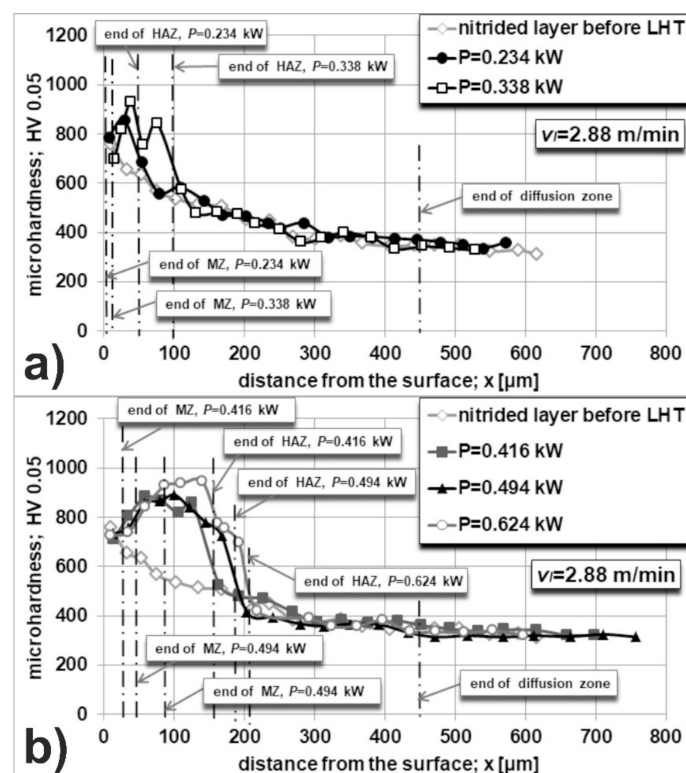

Figure 9. Microhardness profiles in single laser tracks produced on gas-nitrided 42CrMo4 steel using a scanning rate v_l = 2.24 m·min^{-1} and different laser beam powers: P = 0.260 kW and P = 0.364 kW.

The five microhardness profiles of single laser tracks are shown in Figure 10, in which the effect of the temperature distribution is presented after LHT using the scanning rate v_l = 2.88 m·min^{-1}. The laser beam power ranged from 0.234 to 0.624 kW. The two first values of P (0.234 and 0.338 kW) caused the formation of partially re-melted compound zone and heat-affected zone (Figure 10a). The microhardness of relatively thin MZ (partially re-melted iron nitrides) was equal to 787 and 698 HV, respectively. The microhardness of the relatively thin HAZ, produced at the lower laser beam power (0.234 kW) ranged from 689.1 to 857.2 HV, whereas the LHT using the higher value of P (0.338 kW), resulted in the larger depth of HAZ and the microhardness in the range of 752.5–927.2 HV. Like previously, the relatively high microhardness of HAZ was caused by the presence of fine-grained nitric martensite and increased hardenability because of the nitrogen, dissolved in austenite during heating. The presence of coarse-grained nitric martensite in partially re-melted compound zone was the reason for the lower microhardness in this zone. The rest of the microhardness profiles of single laser tracks, produced at a scanning rate of 2.88 m·min^{-1}, are presented in Figure 10b. The laser beam power was in the range of 0.416–0.624 kW. In these cases, the completely re-melted compound zones (MZ) as well as heat-affected zones (HAZ) were clearly visible in the microstructure. The depths of MZ and HAZ increased with the increasing laser beam power. Like previously, the microhardness of MZ was slightly lower than that of HAZ by the reasons, mentioned above. The values, measured in MZ after the LHT using laser beam power of 0.416, 0.494 and 0.624 kW, were as follows: 710 HV, in the range of 732.6–758 HV and in the range of 726.1–841 HV, respectively. Whereas the microhardness of HAZ obtained the values in the range of 802.3–882.5, 726.1–891.2, and 695–936.5 HV after LHT using laser beam power of 0.416, 0.494, and 0.624 kW, respectively.

The microhardness profiles of single laser tracks, produced in the gas-nitrided 42CrMo4 steel at scanning rate v_l = 3.84 m·min^{-1} and the laser beam power in the range of 0.234–0.598 kW are shown in Figure 11. The use of P = 0.234 kW resulted in the formation of a laser track without visible remelting

of compound zone. The microstructure consisted of the laser-modified $\varepsilon + (\varepsilon + \gamma')$ compound zone and heat-affected zone. Figure 11a shows the microhardness measured along the axis of this laser track. The microhardness of the compound zone (965.4 HV) was higher than the value obtained directly after gas nitriding (759.4 HV). It could be the result of an advantageous influence of LHT without remelting on the microstructure of a compound zone. It was reported previously that the outer ε zone seemed to be less porous and more compact because of laser irradiation without remelting [27,28]. The higher hardness of the compound zone after LHT could confirm this conclusion. The microhardness of HAZ ranged from 695 to 865.6 HV and was significantly increased when compared to the same area of diffusion zone in gas-nitrided layer. The slightly increased microhardness was also observed below HAZ up to a depth of 90 μm. It could indicate that the real depth of HAZ was greater. The laser beam power of 0.286 kW caused the formation of partially re-melted compound zone and heat-affected zone. In this case, the microhardness of MZ (557.2 HV) was lower than that of a compound zone directly after gas nitriding (Figure 11a), whereas the microhardness of HAZ was exceptionally high, obtaining the values in the range of 891.2–946 HV. The last microhardness profile, presented in Figure 11a, was determined after LHT with the use of laser beam power $P = 0.390$ kW. In this case, the completely re-melted compound zone and the larger heat-affected zone were identified in the microstructure. Simultaneously, the relatively low microhardness was measured in the MZ (483.4 HV). The HAZ was characterized by the high microhardness, ranged from 841 to 975.4 HV. The relatively thin MZ, slightly bonded to the HAZ, as well as the lower cooling rate could be the probable reasons for the significantly diminished microhardness of MZ in the two last cases.

Figure 10. Microhardness profiles in single laser tracks produced on gas-nitrided 42CrMo4 steel using a scanning rate $v_l = 2.88$ m·min^{-1} and different laser beam powers: $P = 0.234$ kW and $P = 0.338$ kW (**a**); $P = 0.416$ kW, $P = 0.494$ kW, and $P = 0.624$ kW (**b**).

Figure 11b shows the microhardness profiles vs., the distance from the surface, measured after LHT using the scanning rate of 3.84 m·min^{-1} and the next laser beam powers: $P = 0.520$ kW, $P = 0.572$ kW, and $P = 0.598$ kW. In all theses cases, the completely re-melted compound zones as well as the relatively thick heat-affected zones were observed in the microstructure. The use of $P = 0.520$ kW resulted in the

microhardness of MZ in the range of 607.9–766.3 HV and was comparable to the microhardness of compound zone, measured directly after gas nitriding. Like in the previous cases, the HAZ was harder because of the presence of fine-grained nitric martensite with γ' precipitates. The microhardness of HAZ ranged from 726.1 to 946 HV and was significantly increased in comparison with the same area of diffusion zone after gas nitriding. After LHT with the use of laser beam power of 0.572 kW, the measured microhardness of MZ and HAZ ranged from 689.1 to 719.8 HV and from 865.6 to 955.7 HV, respectively. The laser track, produced at $P = 0.598$ kW, was characterized by the relatively high microhardness of MZ (732.6–833 HV) and still higher microhardness of HAZ (908.9–975.4 HV). However, the range of the microhardness, obtained in the MZ and HAZ, could be random to a certain degree. The measured values strongly depended on the selected measuring sites.
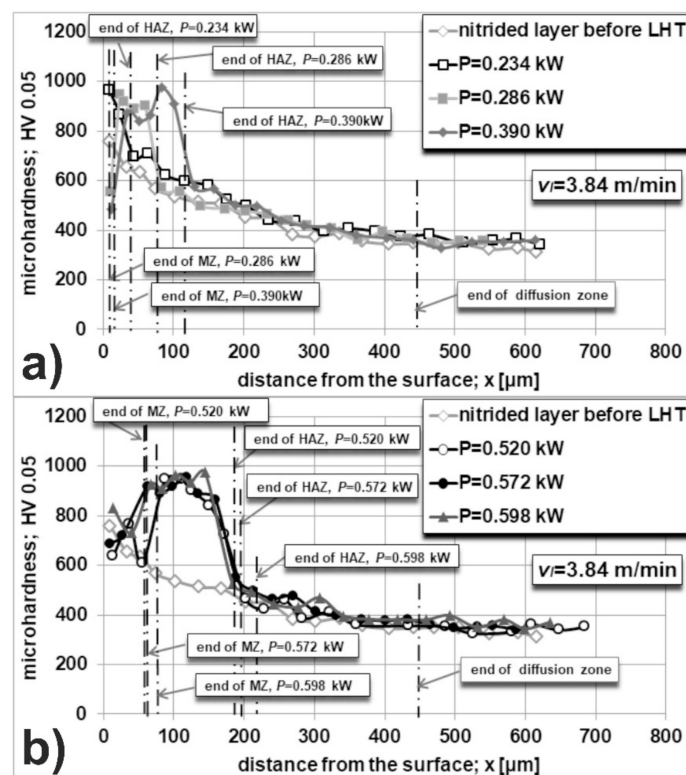
Figure 11. Microhardness profiles in single laser tracks produced on gas-nitrided 42CrMo4 steel using a scanning rate $v_l = 3.84$ m·min^{-1} and different laser beam powers: $P = 0.234$ kW, $P = 0.286$ kW, and $P = 0.390$ kW (**a**); $P = 0.520$ kW, $P = 0.572$ kW, and $P = 0.598$ kW (**b**).

3.4. Effect of the Temperature Distribution on Nanomechanical Properties

Nanomechanical properties were measured for the gas-nitrided layer and the two hybrid surface layers, i.e., gas-nitrided and laser-modified. The selected laser tracks represented the LHT without remelting ($P = 0.234$ kW and $v_l = 3.84$ m·min^{-1}) as well as LHT with significant remelting ($P = 0.624$ kW and $v_l = 2.88$ m·min^{-1}). The measurements were performed on the etched specimens so that it was easy to identify the zones, occurring in the surface layer, as well as the indents in these zones. In the case of gas-nitrided sample, the zones were as follows: compound zone, i.e., ε iron nitrides and $\varepsilon + \gamma'$ iron nitrides, and diffusion zone with nitric sorbite and γ' precipitates. The LHT without remelting provided the microstructure consisted of laser-modified compound zone, i.e., ε iron nitrides and $\varepsilon + \gamma'$ iron nitrides, heat-affected zone with fine-grained nitric martensite and γ' precipitates, and the rest part of the diffusion zone with nitric sorbite and γ' precipitates. Whereas, the LHT with remelting caused the formation of re-melted zone with coarse-grained nitric martensite, heat-affected zone with fine-grained nitric martensite and γ' precipitates, and the rest part of the diffusion zone with nitric

sorbite and γ′ precipitates. The number of measurements in each zone ranged from 3 to 11, depending on the size of the specified zone, i.e., its depth. The nanomechanical properties of the substrate, i.e., quenched and high-temperature tempered 42CrMo4 steel, were also measured. The indentation hardness H_{IT} and plane-strain modulus E^* were provided directly by the nanoindenter, based on the obtained indentation curve (load-displacement curve) during loading and unloading. The Vickers hardness HV_{IT} and indentation modulus E_{IT} were calculated using the equations reported by the paper [28]. The calculations of E_{IT} values required to take into account Poisson's ratio of the measured phase. According to the analysis, mentioned in Section 2.5, Poisson's ratio $\nu_s = 0.3029$ was accepted for calculations in the ε zone, and $\nu_s = 0.3281$ was accepted for ε + γ′ zone. The standard value of Poisson's ratio $\nu_s = 0.3$ was assumed for the other zones, i.e., diffusion zone, re-melted zone, heat-affected zone, as well as substrate material.

Figure 12 shows the selected indentations performed directly after gas nitriding, before LHT. The indentations 1 and 2 were impressed in the zone with ε iron nitrides. The indentation 3 was performed in ε + γ′ iron nitrides. The SEM images of indentations are visible in the upper part of Figure 12. The penetration depth and load vs. time of the test, as well as the load vs. penetration depth (load-displacement curves), are also shown for the three analyzed indents. Based on these curves, the indentation hardness (H_{IT}) and plane-strain modulus E^* were determined. As a consequence, the Vickers hardness HV_{IT} and indentation modulus could be calculated. The SEM images of indents, obtained in a laser track after LHT without remelting ($P = 0.234$ kW and $v_l = 3.84$ m·min^{-1}) as well as corresponding curves are shown in Figure 13. The indentations 4 and 5 corresponded to ε iron nitrides and ε + γ′ mixture of iron nitrides, respectively. The indentation 6 was performed in the HAZ, i.e., in the laser-quenched part of diffusion zone, right below the compound zone. Nitric martensite with γ′ precipitates was characteristic of the microstructure in this zone.
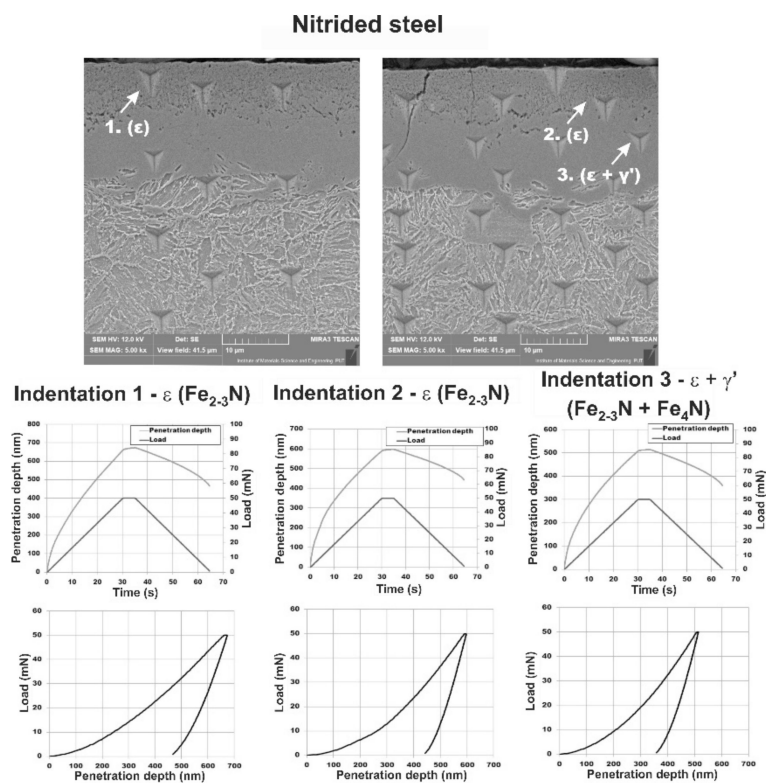
Figure 12. SEM images of indentations and the corresponding curves in gas-nitrided layer: ε (Fe$_{2-3}$N) iron nitrides—indentations 1 and 2, ε + γ′ (Fe$_{2-3}$N + Fe$_4$N) mixture of iron nitrides—indentation 3.
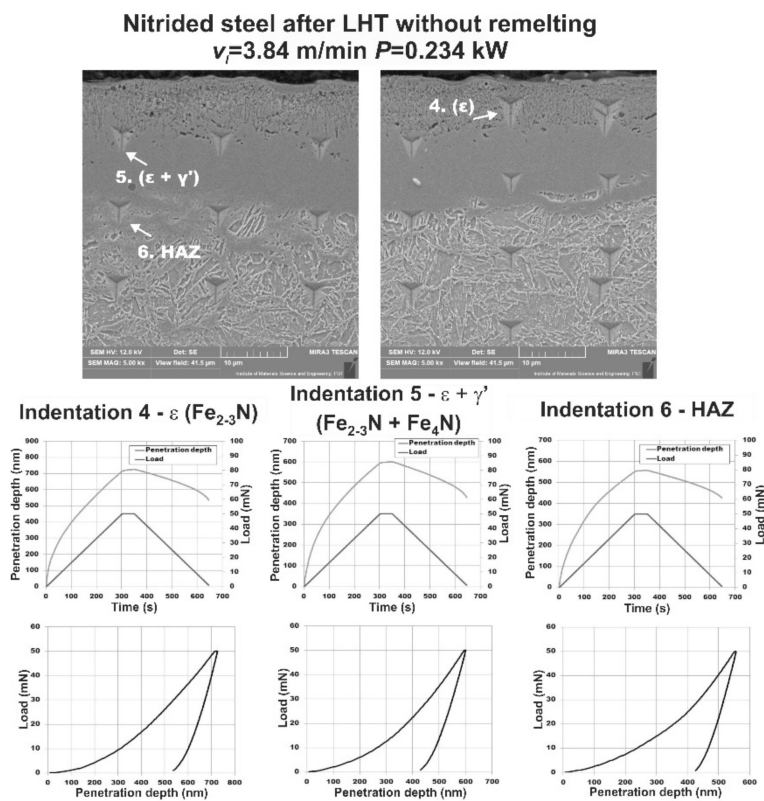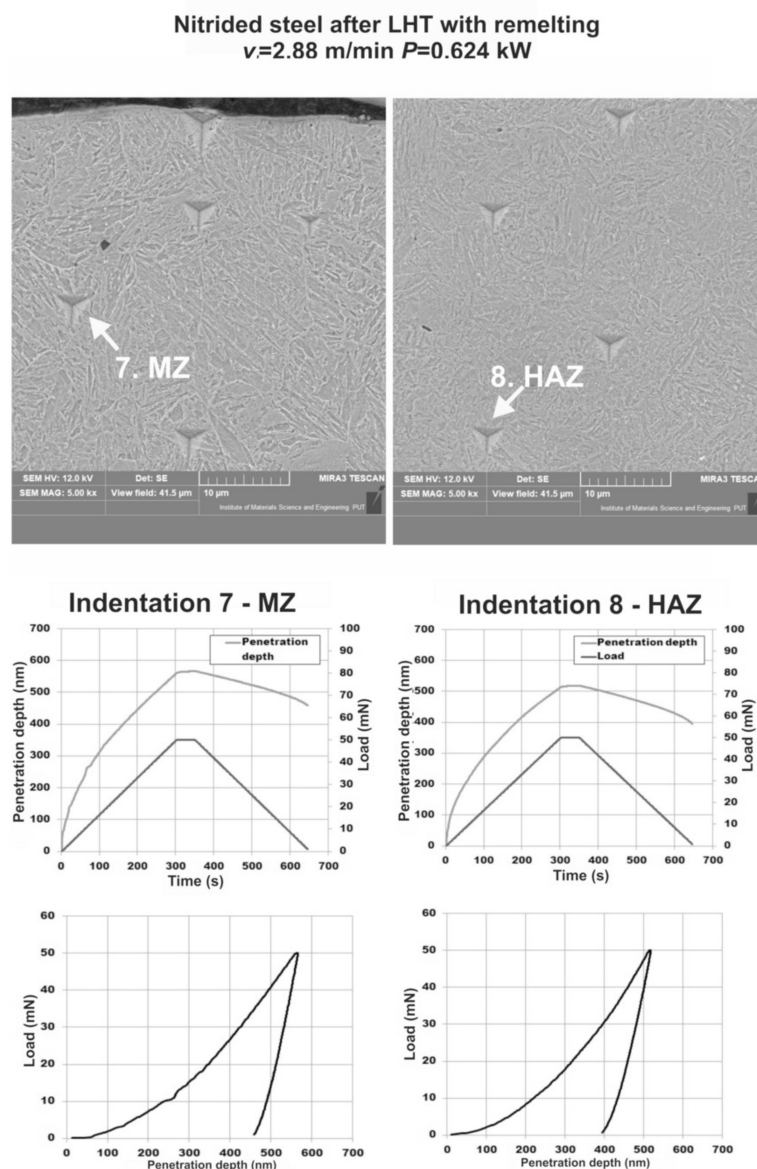
Figure 13. SEM images of indentations and the corresponding curves after gas-nitriding and LHT without remelting (P = 0.234 kW and v_l = 3.84 m·min^{-1}): ε (Fe$_{2-3}$N) iron nitrides—indentation 4, $\varepsilon + \gamma'$ (Fe$_{2-3}$N + Fe$_4$N) mixture of iron nitrides—indentation 5, heat-affected zone (HAZ)—indentation 6.

Figure 14 presents the SEM images of selected indents, performed in a laser track after LHT with remelting (P = 0.624 kW and v_l = 2.88 m·min^{-1}), as well as the recorded curves (penetration depth and load vs., time of the test or load-displacement curves). The indentations 7 and 8 corresponded to MZ and HAZ, respectively. The elastic-plastic behavior of the investigated phases was confirmed by all the indentation curves obtained. The results of the investigations are listed in Table 3 for all the indentations selected. The values of Vickers hardness (HV_{IT}) and indentation modulus (E_{IT}) are shown for gas-nitrided layer and the same layer subjected to LHT with or without re-melting.

Table 3. Some measured HV_{IT} and E_{IT} values in gas-nitrided layer and gas-nitrided layer after LHT with or without remelting.

| Type of Layer	Scanning Rate v_l (m·min^{-1})	Laser Beam Power P (kW)	Indentation	Zone of Measurement	Hardness HV_{IT}	Young's Modulus E_{IT} (GPa)
Nitrided layer	–	–	1	ε	584.85	107.20
			2	ε	633.45	138.21
			3	$\varepsilon + \gamma'$	975.26	186.59
Nitrided layer after LHT without remelting	3.84	0.234	4	ε	562.44	135.23
			5	$\varepsilon + \gamma'$	982.07	203.08
			6	HAZ	891.58	230.53
Nitrided layer after LHT with remelting	2.88	0.624	7	MZ	745.25	231.78
			8	HAZ	913.27	249.59

Figure 14. SEM images of indentations and the corresponding curves after gas-nitriding and LHT with remelting (P = 0.624 kW and v_l = 2.88 m·min^{-1}): re-melted zone (MZ)—indentation 7, heat-affected zone (HAZ)—indentation 8.

The profiles of Vickers hardness HV_{IT} and indentation modulus E_{IT} vs., the distance from the surface in the selected single laser tracks, produced using LHT with and without remelting, are presented in Figures 15 and 16, respectively. The results were compared to the profiles of HV_{IT} and E_{IT} in the gas-nitrided layer. The measurements of HV_{IT}, performed directly after gas nitriding (Figure 15a), revealed the differences in hardness between the ε and $\varepsilon + \gamma'$ zones due to the relatively low load used (50 mN). The details were visible in Figure 15b, in which the results were shown close to the surface up to a depth of 100 μm. HV_{IT} values ranged from 500.5 to 602 HV in the outer zone with ε iron nitrides, whereas the $\varepsilon + \gamma'$ zone was characterized by Vickers hardness HV_{IT} in the range of 984.5–1013.6 HV. Next, the HV_{IT} values gradually diminished in the diffusion zone (composed of nitric sorbite with γ' precipitates) from 580.1 HV directly below the iron nitrides to 382 HV at the end of this zone. The averaging Vickers hardness of the substrate with sorbite was 355.1 HV. The similar HV_{IT} values (Figure 15) were obtained in the compound zone after LHT without remelting (P = 0.234 kW, v_l = 3.84 m·min^{-1}). In this case, the HV_{IT} of ε iron nitrides was in the range of 491.3–676.8 HV, and

the measurements in ε + γ′ zone ranged from 839 to 1088.5 HV (Figure 15b). It was characteristic of the single track, produced without remelting, that the maximal values of HV_{IT} in ε and ε + γ′ zones were higher than those-measured in the gas-nitrided layer. It could indicate an advantageous influence of the LHT without remelting on the microstructure of compound zone. The previous papers [27,28] confirmed the diminished porosity of ε iron nitrides in the case of multiple laser tracks (with overlapping of 72%), formed by LHT without remelting. In the HAZ, the Vickers hardness HV_{IT} obtained the values in the range of 806.8–860.2 HV because of the hardening of this zone by laser quenching. The hardness of this zone was higher than the hardness of the same area of diffusion zone in gas-nitrided layer due to the presence of fine-grained nitric martensite with γ′ precipitates. Below the HAZ (Figure 15a), the values of HV_{IT} gradually decreased from 701.3 to 390 HV in the diffusion zone without laser heat treatment. The Vickers hardness of the substrate material was about 350.1 HV. The use of the laser processing parameters ($P = 0.624$ kW, $v_l = 2.88$ m·min^{-1}), which caused complete remelting of the compound zone, resulted in the Vickers hardness HV_{IT} in the range of 660.6–765.3 HV in MZ and 826.2–1006.9 HV in HAZ. The HV_{IT} hardness of MZ was slightly lower in comparison with the typical microhardness measurements at a load of 0.49 N (726.1–841 HV). Whereas the HV_{IT} values, measured in HAZ, were slightly higher than those-measured at 0.49 N (695–936.5 HV). However, in general, the obtained results were compatible.
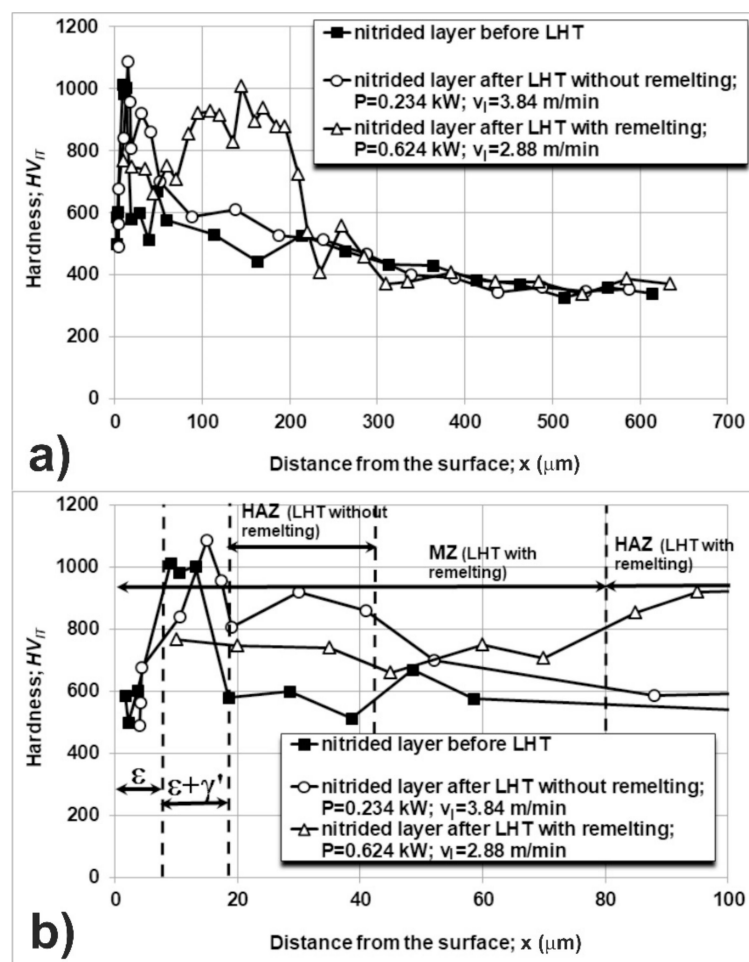
Figure 15. Profiles of Vickers hardness HV_{IT} in the selected single laser tracks after LHT of gas-nitrided layer with or without remelting compared to the gas-nitrided layer: HV_{IT} profiles in the entire layers (**a**); HV_{IT} profiles close to the surface (**b**).
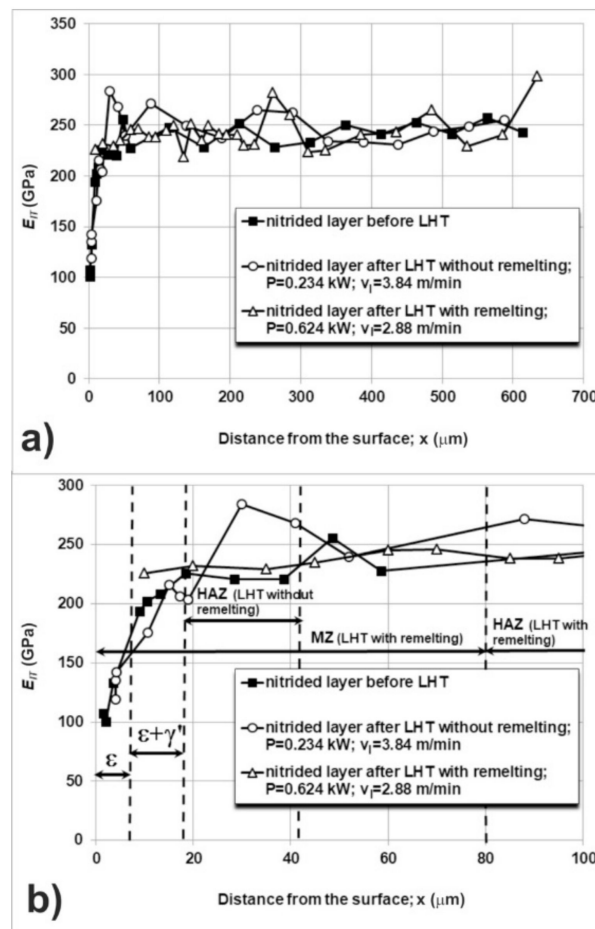
Figure 16. Profiles of indentation modulus E_{IT} in the selected single laser tracks after LHT of gas-nitrided layer with or without remelting compared to the gas-nitrided layer: E_{IT} profiles in the entire layers (**a**); E_{IT} profiles close to the surface (**b**).

The profiles of indentation modulus E_{IT} vs., the distance from the surface in the selected single laser tracks, produced using LHT with and without remelting, are presented in Figure 16a for the entire surface layers. The results were compared to the profile of E_{IT} in the gas-nitrided layer. In general, the significant differences in the values of E_{IT} were visible only in the case of the compound zone, produced by gas nitriding or by gas nitriding and LHT without remelting. The measurements of E_{IT}, performed directly after gas nitriding (Figure 16), revealed the differences in indentation modulus between the ε and $\varepsilon + \gamma'$ zones. The details were visible in Figure 16b, in which the results were shown close to the surface up to a depth of 100 μm. E_{IT} values ranged from 100.7 to 132.9 GPa in the outer zone with ε iron nitrides. Whereas the $\varepsilon + \gamma'$ zone was characterized by indentation modulus E_{IT} in the range of 194.5–208.6 GPa. Next, the E_{IT} values were nearly the same in the diffusion zone (averaging value of 235.7 GPa) as well as the substrate material (averaging value of 247.1 GPa). The similar E_{IT} values (Figure 16) were obtained in the compound zone after LHT without remelting ($P = 0.234$ kW, $v_l = 3.84$ m·min^{-1}). In this case, the indentation modulus E_{IT} of ε iron nitrides was in the range of 119–142.4 GPa, and the measurements in $\varepsilon + \gamma'$ zone ranged from 175.9 to 215.8 GPa (Figure 16b). It was characteristic of the single track, produced without remelting, that the maximal values of E_{IT} in ε and $\varepsilon + \gamma'$ zones were higher than those-measured in the gas-nitrided layer. It confirmed an advantageous influence of the LHT without remelting on the microstructure of a compound zone [27,28]. In the HAZ, the indentation modulus E_{IT} obtained the values in the range of 203.8–284 GPa because of the hardening of this zone by laser quenching. The indentation modulus of this zone was higher than the E_{IT} values of the same area of diffusion zone in gas-nitrided layer due to the presence of fine-grained
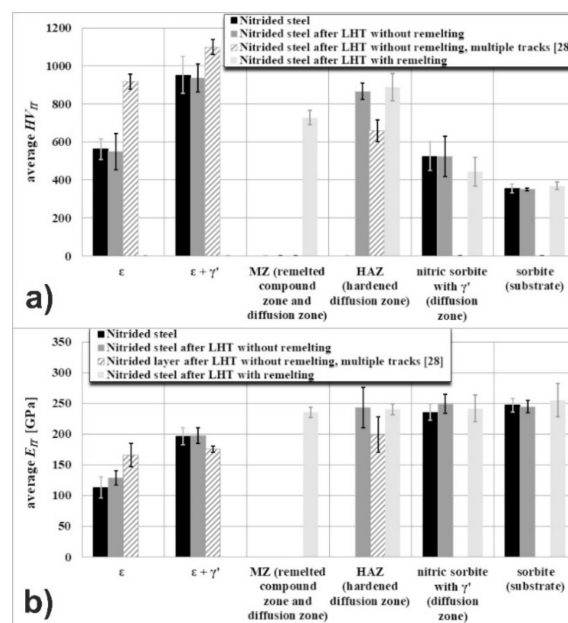
nitric martensite. Below the HAZ (Figure 16a), the values of E_{IT} were in the range of 233.4–271.8 GPa in the diffusion zone without laser heat treatment. The averaging indentation modulus of the substrate material was equal to 244.7 GPa. The use of the LHT with remelting ($P = 0.624$ kW, $v_l = 2.88$ m·min^{-1}), resulted in the indentation modulus E_{IT} in the range of 226–246.2 GPa in MZ and 218.7–250.9 GPa in HAZ. The averaging E_{IT} values in diffusion zone and in the substrate material were equal to 241.6 and 255.2 GPa, respectively.

The averaging values of the Vickers hardness HV_{IT} and indentation modulus E_{IT}, measured in the different zones of gas-nitrided and laser-modified nitrided layers, are listed in Table 4 and shown in Figure 17 with the standard deviations. The results of the present study were compared to the values of HV_{IT} and E_{IT}, obtained after LHT of gas-nitrided layer without remelting in the case of multiple laser tracks' formation with the overlapping of 72% [28].

Table 4. Averaging HV_{IT} and E_{IT} values in nitrided layer, nitrided layer after LHT without remelting, and nitrided layer after LHT with remelting and their standard deviations compared to the previous results.

Type of the Layer	Scanning Rate v_l (m·min^{-1})	Laser Beam Power P (kW)	Zone of Measurement	Averaging Hardness HV_{IT}	Averaging Young's Modulus E_{IT} (GPa)
Nitrided layer (this work)	–	–	ε	562.44 ± 54	113.60 ± 17
			$\varepsilon + \gamma'$	951.51 ± 97	196.92 ± 14
			Nitric sorbite with γ' (diffusion zone)	525.43 ± 77	235.66 ± 13
			Sorbite (substrate)	355.09 ± 23	247.06 ± 11
Nitrided layer after LHT without remelting (single track, this work)	3.84	0.234	ε	549.03 ± 95	129.15 ± 12
			$\varepsilon + \gamma'$	936.44 ± 75	197.99 ± 13
			HAZ	866.53 ± 42	242.92 ± 33
			Nitric sorbite with γ' (diffusion zone)	523.86 ± 106	249.12 ± 15
			Sorbite (substrate)	350.13 ± 6.3	244.70 ± 10
Nitrided layer after LHT with remelting (single track, this work)	2.88	0.624	MZ	727.87 ± 38	235.56 ± 8.5
			HAZ	887.27 ± 72	240.61 ± 9.0
			Nitric sorbite with γ' (diffusion zone)	443.85 ± 76	241.64 ± 22
			Sorbite (substrate)	368.67 ± 20	255.24 ± 27
Nitrided layer after LHT without remelting (multiple tracks) [28]	2.02	0.130	ε	916.79 ± 41	165.72 ± 19
			$\varepsilon + \gamma'$	1098.86 ± 40	175.27 ± 4.8
			HAZ	658.55 ± 57	199.06 ± 29

Figure 17. Averaging values of Vickers hardness HV_{IT} (**a**) and indentation modulus E_{IT} (**b**) and their standard deviations, determined in the different zones of the microstructure.

This study provided the new experimental data related to the indentation moduli (E_{IT}) and Vickers hardness (HV_{IT}) of ε-Fe$_{2-3}$N iron nitride (Table 4). This phase was observed close to the surface in the compound zone after gas nitriding as well as after nitriding followed by laser heat treatment without re-melting using P = 0.234 kW and v_l = 3.84 m·min^{-1}. The controlled gas nitriding resulted in the formation of ε phase, which was characterized by average indentation modulus E_{IT} of 113.60 ± 17 GPa and average Vickers hardness HV_{IT} of 562.44 ± 54 (corresponding to indentation hardness H_{IT} = 6.07 ± 0.6 GPa). These values were slightly lower than those-measured previously (E_{IT} = 123.30 ± 20 GPa and H_{IT} = 7.38 ± 0.9 GPa) [28]. It could result from the differences in chemical composition of ε-Fe$_{2-3}$N phase (e.g., nitrogen concentration) as well as from the more defected microstructure of this zone produced this time. Taking into account the data of other authors, the measured hardness corresponded rather to the value reported by Weber et al. [49] than to the paper [46], and Young's modulus was significantly lower than that measured from ε-Fe$_3$N$_{1-x}$ phase (E_{IT} = 203 GPa), prepared by a reaction of iron powder in flowing NH$_3$ at 520 °C [46]. Probably, the less porosity of ε phase was the reason for the significantly higher E_{IT} value measured [46].

It seemed that LHT without remelting advantageously influenced the indentation modulus of ε iron nitrides. The average E_{IT} value increased up to 129.15 ± 12 GPa (Table 4), whereas LHT without remelting did not influence the Vickers hardness. HV_{IT} obtained 549.03 ± 95 on average (i.e., H_{IT} = 5.93 ± 1.0 GPa). The previous measurements in ε phase, subjected to LHT without remelting, were carried out in the multiple laser tracks [28]. The laser action on this phase was multiplied because of the high overlapping of laser tracks. Hence, the average indentation modulus E_{IT} and indentation hardness H_{IT} strongly increased up to 165.72 ± 19 GPa and 9.90 ± 0.5 GPa, respectively [28]. The diminished porosity and more compact microstructure (as a consequence of LHT) were the probable reasons for such a situation. In case of single laser track, the laser action on the compound zone was not so strong due to the irradiance profile across the laser beam diameter during LHT using the TEM$_{01*}$ mode of laser beam [50].

The Vickers hardness and indentation moduli were also measured in the mixture of iron nitrides ε + γ′ (Fe$_{2-3}$N + Fe$_4$N), occurring below ε zone (Table 4). The average values were determined for this zone directly after gas nitriding as well as after nitriding followed by LHT without remelting. The calculated mean values of E_{IT} (197.99 ± 13 GPa) and HV_{IT} (936.44 ± 75, corresponding to H_{IT} = 10.11 ± 0.8 GPa) after gas nitriding and LHT without remelting were comparable to the values characteristic of only nitrided steel (E_{IT} = 196.92 ± 14 GPa and HV_{IT} = 951.51 ± 97, corresponding to HIT = 10.28 ± 1.1 GPa). In the case of producing the multiple laser tracks without visible effects of remelting [28], the averaging indentation modulus of ε + γ′ iron nitrides was lower (E_{IT} = 175.27 ± 4.8 GPa), and averaging indentation hardness was higher (H_{IT} = 11.87 ± 0.4 GPa) than the values obtained in the present study. However, there was also difficulty to confirm the essential influence of the LHT without remelting on the mechanical properties of ε + γ′ zone in the case of the formation of multiple laser tracks [28]. Taking into account that the determined indentation moduli in ε + γ′ zone were even higher than the measured (157 GPa) [37] or calculated (in the range of 161.5–197 GPa) [37–41,51] values by other authors in γ′ phase, it could indicate the significant percentage of γ′ iron nitrides in this region. Hence, the porosity of ε + γ′ zone, produced by gas nitriding in the present study, had to be relatively small.

The averaging measured values of indentation modulus and Vickers hardness in HAZ (Table 4) were nearly the same in the case of both LHT without remelting (E_{IT} = 242.92 ± 33 GPa, HV_{IT} = 866.53 ± 42) and LHT with remelting (E_{IT} = 240.61 ± 9.0 GPa, HV_{IT} = 887.27 ± 72). Simultaneously, the obtained values in the case of producing the multiple laser tracks [28] were lower (E_{IT} = 199.06 ± 29 GPa, HV_{IT} = 658.55 ± 57). It could result from the worse conditions of heat removal and the lower cooling rate in this zone during formation of multiple laser tracks. The averaging nanomechanical properties of MZ (Table 4) in single laser track (E_{IT} = 235.56 ± 8.5 GPa, HV_{IT} = 727.87 ± 38) were diminished in comparison with those measured in HAZ. The presence of coarse-grained nitric martensite and worse condition of heat removal (lower cooling rate) in MZ could be the reason for such a situation.

The averaging nanomechanical properties were also determined in diffusion zone, consisting of nitric sorbite with γ' precipitates (Table 4). In the case of indentation modulus E_{IT}, the calculations of averaging values in this zone seemed to be justified because of the approximately constant values, measured vs., the distance from the surface. The averaging E_{IT} values of the diffusion zone in gas-nitrided layer, gas-nitrided layer after LHT without remelting, and gas-nitrided layer after LHT with remelting were similar and equal to 235.66 ± 13, 249.12 ± 15, and 241.64 ± 22 GPa, respectively. The calculations of averaging Vickers hardness in the diffusion zone could not be fully accepted due to the gradual decrease in HV_{IT} values towards the core of steel. As a consequence of the LHT, a part of the diffusion zone was laser-quenched, and the area of appearing this zone was reduced. It was visible, especially in the layer, which was laser heat-treated with remelting. In this case, the HAZ was very large and the diffusion zone was reduced the most. As a consequence, the averaging Vickers hardness of the rest part of diffusion zone was relatively low (HV_{IT} = 443.85 ± 76). The differences in the diffusion zone thickness were smaller for the gas-nitrided layer and gas-nitrided layer subjected to LHT without remelting. Therefore, the obtained averaging values of Vickers hardness were similar (525.43 ± 77 and 523.86 ± 106, respectively). Obviously, the averaging nanomechanical properties of the steel substrate with nitric sorbite were similar, irrespective of the surface treatment (Table 4). The mean values of E_{IT} ranged from 244.70 ± 10 GPa measured below the nitrided layer after LHT without remelting and 247.06 ± 11 GPa measured below the gas-nitrided layer to 255.24 ± 27 GPa measured below the nitrided layer after LHT with remelting. The average values of HV_{IT} were equal to 350.13 ± 6.3, 355.09 ± 23, and 368.67 ± 20, respectively.

4. Discussion

The controlled gas nitriding of 42CrMo4 steel resulted in the formation of the nitrided layer composed of $\varepsilon + (\varepsilon + \gamma')$ compound zone of the thickness of 19.35 mm and diffusion zone with the nitric sorbite and γ' precipitates. The depth of the entire nitrided layer was equal to about 450 μm based on the microstructure observations. The relatively thick compound zone was produced in order to study its microstructure and properties after LHT without remelting.

The laser heat treatment of gas-nitrided layer, depending on the laser processing parameters, resulted in the formation of three types of hybrid surface layers: without remelting of compound zone, with complete remelting of compound zone, and with partial remelting of compound zone. The temperature distribution along the axis of a single laser track depended on the laser processing parameters (laser beam power P, scanning rate v_l, laser beam diameter d) and physical properties of the treated material (material density ρ, thermal conductivity λ, specific heat C_p, thermal diffusivity α). The temperature distribution influenced the microstructure of laser tracks. The depths of re-melted zone (d_{MZ}) and heat-affected zone (d_{HAZ}) could be efficiently predicted using the equations developed by Ashby and Esterling.

The LHT with complete remelting of the compound zone caused the formation of re-melted zone (MZ) with coarse-grained nitric martensite $Fe_{\alpha'}$ and possible ε precipitates, heat-affected zone (HAZ) with fine-grained nitric martensite $Fe_{\alpha'}$, and γ' precipitates, and diffusion zone with nitric sorbite and γ' precipitates. Such a microstructure results in the increase in Young's modulus close to the surface. The hardened zone, including MZ and HAZ, appears in the surface layer. The increase in laser beam power usually extends the depth of hardened zone, i.e., the depths of MZ and HAZ. However, too high laser beam power causes diminished hardness in MZ, especially close to the surface, because of the worse cooling conditions, i.e., diminished cooling rate. It can disadvantageously influence the residual stress distribution and, as a consequence, result in worsening the tribological properties. Such a situation requires applying the limited laser beam power.

Sometimes, the compound zone was partially re-melted and an amount of iron nitrides remained in the MZ, also containing coarse-grained nitric martensite $Fe_{\alpha'}$. The next zones were as follows: heat-affected zone (HAZ) with fine-grained nitric martensite $Fe_{\alpha'}$ and γ' precipitates, and diffusion zone with nitric sorbite and γ' precipitates.

After LHT without remelting, the microstructure consisted of the compound $\varepsilon + (\varepsilon + \gamma')$ zone, heat-affected zone (HAZ) with nitric martensite $Fe_{\alpha'}$, and γ' precipitates and diffusion zone with nitric sorbite and γ' precipitates. The compound zone remains in the surface layer because of the relatively low laser beam power. In the case of producing the single laser track, the microhardness of the compound zone is usually higher than that obtained directly after gas nitriding. It can indicate that the outer ε zone is less porous and more compact because of laser irradiation without remelting. However, the nanomechanical properties of compound zone (H_{VIT} and E_{IT}) in this single laser track only slightly differed from those-measured after gas nitriding. In general, E_{IT} was only slightly higher. Based on previous study [28], the formation of multiple laser tracks without remelting using relatively high overlapping can improve the nanomechanical properties of compound zone in comparison with the only gas-nitrided layer. In general, it is difficult to select appropriate laser processing parameters in order to perform the LHT of a nitrided layer without remelting using TLF 2600 Turbo CO_2 laser (TRUMPF, Poznan, Poland). The range of laser beam powers, which provided such a treatment, is relatively narrow at the usually used scanning rate. The equations, developed by Ashby and Esterling, can help during the design of such a laser heat treatment. In the future, the use of the diode laser TruDiode 3006 (TRUMPF, Poznan, Poland) with another irradiance profile will be also proposed to carry out LHT without remelting.

The temperature distribution influenced the Vickers hardness of laser tracks. The hardness of MZ, measured both at a load of 0.49 N and 50 mN (using Berkovich indenter), has been usually higher than that of ε zone and lower than that of $\varepsilon + \gamma'$ zone when compared to gas-nitrided layer. The hardness of HAZ was higher than that of MZ and that of the same area of diffusion zone in the nitrided layer because of the presence of fine-grained nitric martensite with γ' precipitates after laser quenching. The LHT without remelting, providing the formation of a single laser track, resulted with similar hardness of ε zone and $\varepsilon + \gamma'$ zone in comparison with gas-nitrided layer. However, the increased hardness of the compound zone can be expected in case of formation of multiple laser tracks with relatively high overlapping because of the possible decrease in the porosity of ε zone.

The temperature distribution in laser tracks influenced Young's moduli, measured at a load of 50 mN using Berkovich indenter. Young's modulus of MZ was significantly higher than those characteristic of the compound zone in gas-nitrided layer (both ε and $\varepsilon + \gamma'$ zone) and similar to that of HAZ. The LHT without remelting, providing the formation of a single laser track, resulted with slightly higher Young's modulus of ε zone in comparison with gas-nitrided layer. Whereas such a treatment didn't influence the Young's modulus of $\varepsilon + \gamma'$ zone considerably. In the case of producing the multiple laser tracks, the increase in indentation modulus E_{IT} should be stronger.

5. Conclusions

Low-alloy and medium-carbon 42CrMo4 steel was subjected to controlled gas nitriding with changeable nitriding potential. The nitrided layer was composed of $\varepsilon + (\varepsilon + \gamma')$ compound zone of the thickness of 19.35 mm and diffusion zone with the nitric sorbite and γ' precipitates. Such a diffusion surface treatment was followed by laser heat treatment (LHT) with formation of single laser tracks. The laser tracks were formed using various laser beam powers (in the range of 0.234–0.624 kW) and scanning rates (in the range of 2.24–3.84 m·min^{-1}) and the same laser beam diameter (2 mm). The temperature distribution vs. The distance from the surface was calculated in the axis of each laser track using the equations developed by Ashby and Esterling. The effects of the temperature distribution on the microstructure, microhardness, and some nanomechanical properties (Young's modulus and hardness) were studied.

Considering the microstructure, microhardness profiles and nanomechanical properties of laser heat-treated nitrided layers (H_{VIT} and E_{IT}), the conclusions can be formulated regarding the preferable laser processing parameters after the controlled gas nitriding and the temperature distribution during LHT calculated:

- The LHT with remelting eliminates the compound zone from the surface layer and causes the formation of MZ and HAZ. The increase in Young's modulus was observed in MZ. However, too high laser beam power usually results in diminished hardness of MZ in comparison with HAZ, especially close to the surface because of the worse cooling conditions. Hence, the limited laser beam power should be used during LHT with remelting in order to avoid the disadvantageous residual stress distribution and worsening the tribological properties;

- It is difficult to perform the LHT of a nitrided layer without remelting using TRUMPF TLF 2600 Turbo CO_2 laser because of the relatively narrow range of laser beam powers which cause such a treatment. In the future, the use of the diode laser TruDiode 3006 (TRUMPF, Poznan, Poland) with another irradiance profile will be proposed;

- The LHT without remelting causes only partial hardening the diffusion zone below iron nitrides and formation of HAZ due to the relatively low laser beam power. The microhardness of the compound zone is usually higher than that obtained directly after gas nitriding because of the diminished porosity of the outer ε zone. However, the nanomechanical properties of compound zone (H_{VIT} and E_{IT}) were similar to those measured directly after gas nitriding. Probably, the formation of multiple tracks by LHT without remelting will improve these properties;

- The preferable LHT can be indicated based on the microhardness profiles and measurements of nanomechanical properties (H_{VIT} and E_{IT}). It seems that the most advantageous laser beam powers should not exceed: 0.260 kW at the scanning rate of 2.24 m·min^{-1}, 0.416 kW at the scanning rate of 2.88 m·min^{-1}, and 0.520 kW at the scanning rate of 3.84 m·min^{-1};

- The depths of re-melted zone (d_{MZ}) and heat-affected zone (d_{HAZ}), obtained after LHT with or without remelting, could be efficiently predicted using the equations developed by Ashby and Esterling.

Conflicts of Interest: The authors declare no conflict of interest.

References

1. Mittemeijer, E.J. *Fundamentals of Nitriding and Nitrocarburizing*; Dossett, J., Totten, G.E., Eds.; ASM Handbook: Steel Heat Treating Fundamentals and Processes; ASM International: Materials Park, OH, USA, 2013; Volume 4, pp. 619–646.

2. Małdziński, L.; Tacikowski, J. *ZeroFlow Gas Nitriding of Steels*; Mittemeijer, E.J., Somers, M.A.J., Eds.; Thermochemical Surface Engineering of Steels Improving Materials Performance; Woodhead Publishing: Sawston, UK, 2015; pp. 459–483.

3. Michalski, J.; Tacikowski, J.; Wach, P.; Ratajski, J. Controlled gas nitriding of 40 HM and 38 HMJ steel grades with and without the surface compound layer, composed of iron nitrides. *Maint. Probl.* **2006**, *2*, 43–52.

4. Schwartz, B.; Goehring, H.; Meka, S.R.; Schacherl, R.E.; Mittemeijer, E.J. Pore formation upon nitriding iron and iron-based alloys: The role of alloying elements and grain boundaries. *Metall. Mater. Trans. A* **2014**, *45*, 6173–6186. [CrossRef]

5. Kucharska, B.; Michalski, J.; Wójcik, G. Mechanical and microstructural aspects of G20-steel blades subjected to gas nitriding. *Arch. Civ. Mech. Eng.* **2019**, *19*, 147–156. [CrossRef]

6. Michalski, J.; Wach, P.; Tacikowski, J.; Betiuk, M.; Burdyński, K.; Kowalski, S.; Nakonieczny, A. Contemporary industrial application of nitriding and its modifications. *Mater. Manuf. Process.* **2009**, *24*, 855–858. [CrossRef]

7. Borowski, T.; Brojanowska, A.; Kost, M.; Garbacz, H.; Wierzchoń, T. Modifying the properties of the Inconel 625 nickel alloy by glow discharge assisted nitriding. *Vacuum* **2009**, *83*, 1489–1493. [CrossRef]

8. Roliński, E. Plasma-Assisted Nitriding and Nitrocarburizing of Steel and Other Ferrous Alloys. In *Thermochemical Surface Engineering of Steels Improving Materials Performance*; Mittemeijer, E.J., Somers, M.A.J., Eds.; Woodhead Publishing: Sawston, UK, 2015; pp. 413–457.

9. Frączek, T.; Olejnik, M.; Tokarz, A. Evaluation of plasma nitriding efficiency of titanium alloys for medical applications. *Metalurgija* **2009**, *48*, 83–86.

10. Yan, M.F.; Wang, Y.X.; Chen, X.T.; Guo, L.X.; Zhang, C.S.; You, Y.; Bai, B.; Chen, L.; Long, Z.; Li, R.W. Laser quenching of plasma nitrided 30CrMnSiA steel. *Mater. Des.* **2014**, *58*, 154–160. [CrossRef]

11. Conci, M.D.; Bozzi, A.C.; Franco, A.R., Jr. Effect of plasma nitriding potential on tribological behaviour of AISI D2 cold-worked steel. *Wear* **2014**, *317*, 188–193. [CrossRef]

12. Shen, H.; Wang, L. Influence of temperature and duration on the nitriding behavior of 40Cr low alloy steel in mixture of NH_3 and N_2. *Surf. Coat. Technol.* **2019**, *378*, 124953. [CrossRef]

13. Wołowiec, E.; Kula, P.; Januszewicz, B.; Korecki, M. Mathematical modelling the low-pressure nitriding process. *Appl. Mech. Mater.* **2013**, *421*, 377–383. [CrossRef]

14. Wolowiec-Korecka, E.; Michalski, J.; Kucharska, B. Kinetic aspects of low-pressure nitriding process. *Vacuum* **2018**, *155*, 292–299. [CrossRef]

15. Michalski, J.; Burdyński, K.; Wach, P.; Łataś, Z. Nitrogen availability of nitriding atmosphere in controlled gas nitriding processes. *Arch. Metall. Mater.* **2015**, *60*, 747–754. [CrossRef]

16. Wang, B.; Sun, S.; Guo, M.; Jin, G.; Zhou, Z.; Fu, W. Study on pressurized gas nitriding characteristics for steel 38CrMoAlA. *Surf. Coat. Technol.* **2015**, *279*, 60–64. [CrossRef]

17. Ratajski, J. Relation between phase composition of compounded zone and growth kinetics of diffusion zone during nitriding of steel. *Surf. Coat. Technol.* **2009**, *203*, 2300–2306. [CrossRef]

18. Ratajski, J.; Suszko, T. Modeling of the nitriding process. *J. Mater. Process. Technol.* **2008**, *195*, 212–217. [CrossRef]

19. Bojinović, M.; Mole, N.; Štok, B. A computer simulation study of the effects of tempearture change rate on austenite kinetic in laser hardening. *Surf. Coat. Technol.* **2015**, *273*, 60–76. [CrossRef]

20. Major, B. Laser processing for surface modification by remelting and alloying of metallic system. In *Materials Surface Processing by Directed Energy Techniques*; Yves, P., Ed.; Elsevier: Oxford, UK, 2006.

21. Safdar, S.; Li, L.; Sheikh, M.A.; Liu, Z. An analysis of the effect of laser beam geometry on laser transformation hardening. *J. Manuf. Sci. Eng.* **2006**, *128*, 659–667. [CrossRef]

22. Steen, P.H.; Ehrhard, P.; Schussler, A. Depth of melt-pool and heat-affected zone in laser surface treatments. *Metall. Mater. Trans. A* **1994**, *25*, 427–435. [CrossRef]

23. Antonov, V.; Iordanova, I. Development and application of a numerical model for characterization of thermal fields during surface laser treatment of solid materials. *Bulg. J. Phys.* **2007**, *34*, 295–306.

24. Kim, J.-D.; Lee, M.-H.; Lee, S.-J.; Kang, W.-J. Laser transformation hardening on rod-shaped carbon steel by Gaussian beam. *Trans. Nonferr. Metal. Soc.* **2009**, *19*, 941–945. [CrossRef]

25. Sherchiff, H.R.; Ashby, M.F. The prediction of case depth in laser transformation hardening. *Metall. Mater. Trans. A* **1991**, *22*, 2459–2466. [CrossRef]

26. Yanez, A.; Alvarez, J.C.; Lopez, A.J.; Nicolas, G.; Perez, J.A.; Ramil, A.; Saavedra, E. Modelling of temperature evolution on metals during laser hardening process. *Appl. Surf. Sci.* **2002**, *186*, 611–616. [CrossRef]

27. Kulka, M.; Panfil, D.; Michalski, J.; Wach, P. The effects of laser surface modification on the microstructure and properties of gas-nitrided 42CrMo4 steel. *Opt. Laser Technol.* **2016**, *82*, 203–219. [CrossRef]

28. Panfil, D.; Kulka, M.; Wach, P.; Michalski, J.; Przestacki, D. Nanomechanical properties of iron nitrides produced on 42CrMo4 steel by controlled gas nitriding and laser heat treatment. *J. Alloys Compd.* **2017**, *706*, 63–75. [CrossRef]

29. Kulka, M.; Panfil, D.; Michalski, J.; Wach, P. Modelling of the effects of laser modification of gas-nitrided layer. *Arch. Mater. Sci. Eng.* **2017**, *88*, 59–67. [CrossRef]

30. Panfil, D.; Kulka, M.; Wach, P.; Michalski, J. Microstructure and wear resistance of gas-nitrided 42CrMo4 steel after laser modification. *J. Achiev. Mater. Manuf. Eng.* **2017**, *85*, 12–20.

31. Ashby, M.F.; Esterling, K.E. The transformation hardening of steel surfaces by laser beams—I. Hypo-eutectoid steels. *Acta Metall.* **1984**, *32*, 1935–1948. [CrossRef]

32. Ion, J.C.; Esterling, K.E.; Ashby, M.F. A second report on diagrams of microstructure and hardness for heat-affected zones in welds. *Acta Metall.* **1984**, *32*, 1949–1962. [CrossRef]

33. Li, W.B.; Esterling, K.E.; Ashby, M.F. The transformation hardening of steel—II. Hypereutectoid steels. *Acta Metall.* **1986**, *34*, 1533–1543. [CrossRef]

34. Makuch, N.; Dziarski, P.; Kulka, M. The effect of laser treatment parameters on the temperature distribution and thickness of laser-alloyed layers produced on Nimonic 80A-alloy. *J. Achiev. Mater. Manuf.* **2017**, *83*, 67–78. [CrossRef]

35. Chełmińska, H. Characteristics of steel. In *Alloy Constructional Steels, Steels for the Quenching and Tempering*; Institute of Ferrous Metallurgy; Publishing House: Gliwice, Poland, 1975; Volume 1. (In Polish)

36. Oliver, W.C.; Pharr, G.M. An improved technique for determining hardness and elastic modulus using load and displacement sensing indentation experiments. *J. Mater. Res.* **1992**, *7*, 1564. [CrossRef]

37. Takahashi, T.; Burghaus, J.; Music, D.; Dronskowski, R.; Schneider, J.M. Elastic properties of γ'-Fe$_4$N probed by nanoindentation and ab initio calculation. *Acta Mater.* **2012**, *60*, 2054–2060. [CrossRef]

38. Chen, J.S.; Yu, C.; Lu, H. Phase stability, magnetism, elastic properties and hardness of binary iron nitrides from first principles. *J. Alloys Compd.* **2015**, *625*, 224–230. [CrossRef]

39. Cheng, C.-H.; Nguyen, M.-T.; Leu, T.-S.; Chang, I.-L.; Liao, M.-L.; Panin, S.V.; Panin, A.V. Magnetic and mechanical properties of deformed iron nitride γ'-Fe$_4$N. *J. Appl. Math.* **2015**. [CrossRef]

40. Gressmann, T.; Wohlschlögel, M.; Shang, S.; Welzel, U.; Leineweber, A.; Mittemeijer, E.J.; Liu, Z.-K. Elastic anisotropy of γ'-Fe$_4$N and elastic grain interaction in γ'-Fe$_4$N$_{1-y}$ layers on γ'-Fe: First-principles calculations and diffraction stress measurements. *Acta Mater.* **2007**, *55*, 5833–5843. [CrossRef]

41. Zhao, E.; Xiang, H.; Meng, J.; Wu, Z. First-principles investigation on the elastic, magnetic and electronic properties of MFe$_3$N (M=Fe, Ru, Os). *Chem. Phys. Lett.* **2007**, *449*, 96–100. [CrossRef]

42. Zhang, C.S.; Yan, M.F.; You, Y.; Chen, H.T.; Zhang, F.Y.; Bai, B.; Chen, L.; Long, Z.; Li, R.W. Stability and properties of alloyed ε-(Fe$_{1-x}$M$_x$)$_3$N nitrides (M = Cr, Ni, Mo, V, Co, Nb, Mn, Ti and Cu): A first-principles calculations. *J. Alloys Compd.* **2014**, *615*, 854–862. [CrossRef]

43. Shi, Y.J.; Du, Y.-L.; Chen, G. First-principles study on the elastic and electronic properties of hexagonal ε-Fe$_3$N. *Comput. Mater. Sci.* **2013**, *67*, 341–345. [CrossRef]

44. Zhang, W.H.; Lv, Z.Q.; Shi, Z.P.; Sun, S.H.; Wang, Z.H.; Fu, W.T. Eletronic, magnetic and elastic properties of ε-phase Fe$_3$X (X = B, C,N) from density functional theory calculation. *J. Magn. Magn. Mater.* **2012**, *324*, 2271–2276. [CrossRef]

45. Gressmann, T.; Leineweber, A.; Mittemeijer, E.J. X-ray diffraction line-profile analysis of hexagonal ε-iron nitride compound layers: Composition—And stress—Depth profiles. *Philos. Mag.* **2008**, *88*, 145–169. [CrossRef]

46. Niewa, R.; Rau, D.; Wosylus, A.; Meier, K.; Hanfland, M.; Wessel, M.; Dronskowski, R.; Dzivenko, D.A.; Riedel, R.; Schwarz, U. High pressure-high temperature single crystal growth, ab initio electronic structure calculations and equation of state of ε-Fe$_3$N$_{1+x}$. *Chem. Mater.* **2009**, *21*, 392–398. [CrossRef]

47. Technical Card of Lucefin Group According to ISO 683-2: 2018 Standards. 2018. Available online: https://www.lucefin.com/wp-content/files_mf/152353604042CrMo4.pdf (accessed on 8 July 2020).

48. Data of Xingsheng Special Steel Company. Available online: http://www.round-bars.com/products/aisi-4140-steel/ (accessed on 8 July 2020).

49. Weber, T.; Wit, L.; Saris, F.M.; Königer, A.; Rauschenbach, B.; Wolf, G.K.; Krauss, S. Hardness and corrosion resistance of single-phase nitride and carbide on iron. *Mater. Sci. Eng. A* **1995**, *199*, 205–210. [CrossRef]

50. Kulka, M.; Makuch, N.; Pertek, A. Microstructure and properties of laser-borided 41Cr$_4$ steel. *Opt. Laser Technol.* **2013**, *45*, 308–318. [CrossRef]

51. Yan, M.F.; Wu, Y.Q.; Liu, R.L. Plasticity and ab initio characterizations on Fe$_4$N produced on the surface of nanocrystallized 18Ni-maraging steel plasma nitrided at lower temperature. *Appl. Surf. Sci.* **2009**, *255*, 8902–8906. [CrossRef]